This is a repository copy of *Hydrogen embrittlement mechanisms in advanced high strength steel*.

White Rose Research Online URL for this paper:
https://eprints.whiterose.ac.uk/186360/

Version: Accepted Version

Hydrogen embrittlement mechanisms in advanced high strength steel

Peng Gong[a], Andrej Turk[b], John Nutter[a], Feng Yu[a], Bradley Wynne[c], Pedro Rivera-Diaz-del-Castillo[d], W. Mark Rainforth[a]

[a] Department of Materials Science and Engineering, University of Sheffield, Sir Robert Hadfield Building, Mappin Street, Sheffield, S1 3JD, UK

[b] OxMet Technologies Ltd, Unit 15, Oxford Business Park, Yarnton, Kidlington, United Kingdom

[c] Mechanical and Aerospace Engineering, University of Strathclyde Glasgow, James Weir Building, 75 Montrose Street, Glasgow, G1 1XJ

[d] Department of Engineering, Lancaster Unviersity, Engineering Building, Lancaster, LA1 4YW

Abstract

Hydrogen embrittlement is increasingly important in advanced high strength steels (AHHS) as strength levels increase well above 1000MPa. This work developed a detailed understanding of the embrittling mechanism in model AHHS steels based on Fe-Ti-Mo and Fe-V-Mo, both strengthened through interphase precipitation. Hydrogen charging led to an increase in the dislocation density and an enlarged strain field around precipitates, resulting in an increase in residual stress. This was much greater for the Ti-Mo steel compared to the V-Mo. Important differences in the hydrogen trapping behaviour was seen between the two steels, with hydrogen believed to be trapped at the matrix/precipitate interface for the Ti-Mo steel, but within the precipitate for the V-Mo steel. The effects of hydrogen were investigated in detail for slow strain rate tensile tests and double notched tensile samples. Hydrogen charging resulted in a loss in strength and ductility, with the Ti-Mo steel failing at yield, while the V-Mo steel exhibited a ~13% loss in strength and a ~ 35% loss of ductility. Crack initiation in tensile samples occurred at high strain gradient dislocation boundaries. However, crack propagation rapidly became quasi-cleavage, along the {100} plane in ferrite, and also along the martensite/ferrite grain boundaries on the {110} plane in the martensite. Minimal plasticity was observed associated with the crack tip, which was believed to be a result of the suppression of dislocation emission at the crack tip by the hydrogen.

Keywords: Hydrogen embrittlement, interphase precipitation, initiation and propagation of cracks.

*Corresponding author: m.rainforth@sheffield.ac.uk

1.Introduction

There has been much drive to increase the strength of steels as part of a strategy to reduce CO_2 emissions through higher performance in, for example, ultra-light car bodies. This has led to the rapid development of Advanced High Strength Steels (AHSS) which provide ever

increasing strength levels, but with excellent ductility. AHSS have several different microstructures including ferrite/martensite dual phase (DP), transformation induced plasticity (TRIP), complex phase (CP) and martensitic steels. DP steels, which offer a tensile strength (around 1.0GPa) and ductility (no less than 10%) are the most attractive AHSS steels for safe and fuel-efficient cars due to the simple production process. As the strength of the steel increases, the susceptibility to hydrogen embrittlement (HE) increases, to the point now that HE is an important consideration in the design of AHSS.

There are numerous observations of HE and many theories have been proposed [1-26]. The contrasting theories of hydrogen embrittlement range from enhanced dislocation mobility leading to failure to suppression of dislocation emission at a crack tip. Hydrogen enhanced localized plasticity (HELP) [19-23] has received extensive attention in the literature and proposes enhanced crack growth is a highly localised plastic failure process as a result of enhanced dislocation emission and mobility. At the opposite end of the spectrum, hydrogen enhanced decohesion (HEDE) considers that atomic bonding is weakened at the crack tip by the presence of hydrogen [24, 25]. However, as Song and Curtin [26] have pointed out, the stress intensity at the crack tip must be lower than the value at which dislocation emission occurs, which is physically unrealistic. Rather, their modelling indicates that the primary role of hydrogen is to suppress dislocation emission from the crack tip, leaving cleavage as the only energy dissipation mechanism available. Some theories are quite specific to the phases present.

There are several studies of HE in DP steels (although not in precipitation hardened DP steels), which show, for example, the ability of a crack to nucleate and grow is a function of strength, size and distribution of the martensite islands after hydrogen charging, as well as the carbon content in the martensite phase [9, 24, 27-30]. Sun et al. [31] reported that with the carbon exceeding 0.15%, HE was associated with crack initiation in the hard martensite regions and

propagates through the ferrite grain or along the ferrite/ martensite interface due to the increase of mobile dislocations by transportation of hydrogen atoms. Koyama et al. [24] reported that in DP steels HE promotes damage nucleation and growth mechanisms, while the ability of ferrite to arrest cracks is greatly reduced. The critical strain for decohesion in the martensite was decreased through the HEDE mechanism, while the cracking in the martensite/ferrite interface and in the ferrite was enhanced through the HELP mechanism. However, there is no research on HE in DP steels strengthened by precipitation, which of course can act as efficient hydrogen traps as well as modifying dislocation dynamics. Moreover, the volume fraction of the martensitic in the current steels is much lower than conventional DP steels.

The present work focuses on a detailed analysis of the hydrogen induced cracking mechanism, looking at both crack initiation and propagation with the effect of volume fraction of martensite, different types and volume fraction of precipitaitons as well as the different density of dislocations. In order to do this, model steel microstructures were developed, comprising fine grained ferrite, precipitation hardened with fine coherent precipitates that are known to act as efficient hydrogen trapping sites. In addition, both steels contained fine martensite islands and high volume fraction of precipitations, with ~5% martensite and TiC in the Ti-Mo steel and ~20% martensite and VC in the V-Mo steel. Both steels exhibit a good combination of strength and ductility. Slow strain rate testing (SSRT) and double notched tensile tests were used to study the HE susceptibility, and the fracture morphology was examined to analyse the nucleation and propagation of hydrogen assisted cracks.

2.Experimental Methods

2.1 Materials

The chemical composition of the laboratory cast Fe-Ti-Mo (Ti-Mo), Fe-V-Mo (V-Mo) steels are listed in Table 1. The alloys were made by vacuum induction melting and cast into ingots

having dimensions 620 mm × 105 mm × 35 mm at Tata Steel, IJmuiden. The ingots were homogenized at 1250 °C for 2 h and hot worked through several passes to 8 mm thick plates. Dilatometer specimens, 120 mm long × 12 mm wide × 6 mm thick, were machined from the plate along the rolling direction. The heat treatment for producing interphase precipitated carbides was performed using the Dilatronic dilatometer at The University of Sheffield. Samples were first reheated to 1250 °C in a tube furnace, held for 30 min, and then water quenched to room temperature. The specimens were then austenitised at 1200 °C for 3 min and rapidly cooled to 630 °C at a rate of 10 °Cs^{-1}, held isothermally for 90 min, and finally water quenched to room temperature. The rolling and heat treatment schedule are illustrated in Fig. 1.

Table 1
Chemical composition of the experimental steels (wt%)

Materials	C	Si	Mn	Al	V	Ti	N	Mo
Ti-Mo	0.1	0.2	1.6	0.045	-	0.2	≤10ppm	0.5
V-Mo	0.1	0.2	1.6	0.045	0.2	-	≤10ppm	0.5

2.2 Hydrogen charging and mechanical tests

Tensile test specimens were prepared according to ASTM standard (E 8M-04) with the long axes parallel to the rolling direction (shown in Fig. 2). Smooth, tensile specimens were 2.66 mm thick with a gauge length of 12.5 mm (Fig. 2 (a)). The double notched tensile specimens were 2.66 mm thick, with a notch of 60°, 1 mm deep and a root radius of 0.15 mm (Fig. 2 (b)). For the double notch tensile samples, failure occurred from one notch, allowing the study of damage accumulation at the second unbroken notch.

Hydrogen charging was undertaken using standard electrochemical techniques. The tensile test specimens were charged using 1 g/L in an aqueous solution of 3 wt% NaCl and 0.3 wt% NH$_4$SCN with a current of 10 mAcm^{-2} at room temperature. Charging was undertaken for 1, 2,

4, 16 and 48h and TDS (thermal desorption spectroscopy) spectra were taken from each to determine the time at which the specimen was saturated with hydrogen (see section 2.3 for TDS procedure). Based on this, all samples for further investigation were charged for 48 h, which was shown to be the fully saturated condition. Following charging, samples were immediately tensile tested using a constant slow strain-rate tensile of 10^{-5} s^{-1} at room temperature using a Zwick (BTC T1-FR020 TN A50) universal testing machine.

2.3 Hydrogen measurement and observation of hydrogen trapping sites

To measure the concentrations of diffusible H in the H-charged specimens, thermal desorption spectroscopy (TDS) was conducted using a gas chromatography system (Agilent Technologies 7890A) and a tubular furnace in a He gaseous atmosphere. The samples was transfer to TDS rig within 10 min after H charging, but purged for 20 min before the start of the TDS experiment. Continuous heating from room temperature to 700 °C was used. Heating rates of 50, 100 and 150 °Ch^{-1} were used to determine the activation energy. The detailed understanding of hydrogen charging was undertaken at a heating rate of 100 ºCh^{-1}.

2.4 Microstructural and crystallographic investigation

Residual stress measurements were made using X-ray diffraction using the sin^2 ψ method [32] on a Siemens D5000. A number of XRD spectra are obtained with the sample systematically tilted through angles, ψ, (in this case, 10 spectra were obtained a different tilt angles). The inter-planar spacing of the chosen crystallographic plane, i.e. the 2Θ peak position, is measured and is plotted against sin^2 ψ. In this case, the (211) plane was selected, since the errors are smaller with the higher angle planes. The strain at an angle ϕ to the principal stress axis σ_1, for a sample tilt ψ, is given by:

$$\epsilon_{\phi\psi} = \frac{1+\upsilon}{E}(\sigma_1 cos^2\phi + \sigma_2 sin^2\phi)sin^2\psi - \frac{\upsilon}{E}(\sigma_1 + \sigma_2) \qquad \text{-(1)}$$

Where υ is Poisson's ratio, σ_1 and σ_2 are the principal stresses along the axes in the sample plane and E is Young's modulus. If the strains are considered in terms of the inter-planar spacing, the stress at an angle ϕ is given by:

$$\sigma_\phi = \frac{E}{(1+v)sin^2\psi}\left(\frac{d_\psi-d_n}{d_n}\right)$$ -(2)

Where d_n is the stress free lattice spacing and d_ψ is the lattice spacing at specimen tilt angle ψ. The residual stress for a given crystallographic plane is then obtained by obtaining the gradient in a plot of d_ψ against $sin^2 \psi$.

The general microstructures of the two steels were examined using a field-emission scanning electron microscope (FE-SEM; FEI NOVA, The Netherlands) equipped with electron backscattered diffraction (EBSD; Oxford Instruments, UK). Specimens for SEM and EBSD observation were prepared by standard metallographic methods which included grinding from P400 to P1200 and polishing up to 0.04 um colloidal silica particles.

EBSD was undertaken on an FEI-Nova 600 at 20 kV with 14 mm working distance. A step size of 150 nm was used for all samples. Post-processing of the EBSD data was undertaken using the Oxford Instruments-channel 5TM software package. The EBSD maps were first cleaned by removing wild orientation spikes, extrapolating zero solution using a minimum of 6 neighbouring pixels. Several orientation imaging microscopy (OIM) maps, namely inverse pole figure (IPF), band contract (BC), kernel average misorientation (KAM), were obtained. Crystal orientation maps were employed to select certain grain orientations from an overall microstructure. The kernel average misorientation, which represents the numerical misorientation average of a given pixel with its neighbours, was used to characterize the local strain distribution in the microstructure and at cracks. The maps were calculated imposing a maximum misorientation of 5 (small local deformations) and with third neighbour

misorientation averaging. Such maps allow a qualitative evaluation of small local strain gradients, since these are related to orientation gradients in the material.

TEM thin foils were obtained by standard electropolishing techniques. Samples were cut from the heat-treated blanks, and ground to about 60 μm using conventional techniques, and then electropolished in a Struers Tenupol Model twin-jet electropolishing unit, using a solution of 50 ml perchloric acid, 600 ml methanol and 350 ml butyl alcohol at a temperature of -40°C. TEM (transmission electron microscopy) samples were also extracted from site-specific locations from the fracture surface using the FIB lift-out technique with the FEI Helios Nanolab 650 SEM/FIB, enabling the examination of deformation microstructures immediately beneath the fracture surface. During the FIB lift-out from the fracture surface, platinum (Pt) was slowly deposited on the location of interest to preserve the corresponding fracture surface at the location and the microstructure below it. TEM studies were conducted in a Philips 420 microscope operating at an accelerating voltage of 120 kV, and a JEOL-F200 microscope TEM/STEM (scanning transmission electron microscopy) operating at an accelerating voltage of 200 kV and a FEI Tecnai Osiris 80 operating at an accelerating voltage of 200 kV.

3. Results
3.1.Microstructure of starting materials
The full details of the microstructure are given in [33]. The optical microstructure of the steels is shown in Fig. 3 (a, b), revealing a predominantly ferritic microstructure with martensite islands. XRD demonstrated the absence of any retained austenite, Fig. A1. The V-Mo samples had a higher volume fraction of martensite (~20%) than the Ti-Mo sample (~5%). The average ferrite grain size of the Ti-Mo steel was 9.7 μm and the V-Mo steel was 19.1 μm.

Representative TEM micrographs complete with diffraction patterns from electropolished samples are shown in Fig. 3 (c-f). Precipitates were present in parallel rows showing classical

interphase precipitation. For the Ti bearing steel, the two types of precipitate were observed throughout the sample, namely TiC (finer) and Ti_2C (coarser), while for the V bearing steels, VC (finer) and V_4C_3 (coarser) were observed. The TiC and VC formed by classical planer interphase precipitation while the Ti_2C and V_4C_3, that had a much wider row spacing, formed through curved interphase precipitation. Each adopted one variant of the Baker-Nutting orientation relationship [33]. The smallest precipitates of both TiC and VC were shown to be fully coherent with the matrix. The larger precipitates were plate-shaped, with the larger interfaces being semicoherent with the matrix. The size distribution of the precipitates is given in Fig. 4. The number density of interphase precipitates in the Ti-Mo steel was 550 ± 38 μm^{-2}, which was slightly larger than in the V-Mo steel with 420 ± 31 μm^{-2}. The average size of the precipitates in the Ti-Mo steel was 5.8 ± 0.1 nm. For the V-Mo steel the average size of the precipitates was 7.9 ± 0.1 nm.

3.2. TDS

TDS was undertaken to investigate the hydrogen trapping behaviour of the two steels. In the first instance hydrogen charging was undertaken for various different times and the TDS spectra are presented in Fig. A2. This demonstrated that after 48 h the sample was fully saturated with hydrogen. Therefore, this charging time was used for all samples for further investigation.

In order to determine the activation energy, E_a, of the hydrogen traps, the standard method was used, based around the simplified form of the original Kissinger [34] equation:

$$\frac{d\left(ln\frac{\phi}{T_{max}^2}\right)}{d\left(\frac{1}{T_{max}}\right)} = -\frac{E_a}{R}$$
-(3)

Where ϕ is the heating rate (K/min), T_{max} is the temperature of the peak in the TDS spectrum, E_a (J/mol) is the detrapping activation energy associated with the peak of interest, and R (JK^{-1} mol^{-1}) is the universal gas constant. TDS was undertaken at heating rates of 50, 100 and 150 °C

h[-1], as shown in Fig. A3. The values of E_a were obtained from a plot of $ln\left(\phi/T_{max}^2\right)$ against $\left(1/T_{max}\right)$. The activation energies measured from these peaks, without any deconvolution to the peaks, is presented in Table 2.

In order to determine the specific microstructural consistent contribution to hydrogen trapping TDS were acquired at a heating rate of 100 ºCh[-1], with the spectra given in Fig. 5. The low temperature peak is associated with several different trapping sites including dislocations, grain boundaries, martensite lath boundaries, coherent precipitates and vacancies, convoluted into a single experimental peak. The activation energies for these trapping sites have been widely reported in the literature and will be discussed later. Following what has now become standard procedure (the procedures are given by Lee & Lee [35] and Depover and Verbeken [36]), the low temperature peak was deconvoluted into three peaks. The results for each steel are presented in Fig. 6 and corresponding activation energies for the different peaks are summarised in Table 2. The hydrogen concentration for each of the simulated peaks was calculated and is shown in Table 3 along with total hydrogen concentration in the low temperature peak.

Table 2.

Activation energy, E_a, measured from the TDS spectra

		E_a (J/mol), Low temperature peak			E_a (J/mol), High temperature peak
	E_a(different heating rate)	Ea1 Simulation Peak 1	Ea2 Simulation Peak 2	Ea3 Simulation Peak 3	
Ti-Mo steel	36.8	18	35	55	73.8
V-Mo steel	25.9	18	35	58	66.9

The second, high temperature, peak for the Ti-Mo steel covered a wider temperature range and with a lower peak temperature than for the V-Mo steel. However, the total hydrogen under the high temperature peak was similar for both steels (0.10±0.01wppm for the Ti-Mo steel and

0.14±0.01wppm for the V-Mo steel), Table 3. The differences in temperature range and peak temperature were probably a result of the differences in precipitate type, discussed later.

Table 3.
Hydrogen concentrations (all wppm) of the deconvoluted low temperature peaks in Figs. 5 and 6

	Experimentally measured total peak H concentration	Simulated peaks within low temperature peak H concentration/wppm			High temperature peak H concentration/wppm
		Peak 1	Peak 2	Peak 3	
Ti-Mo	0.54±0.02	0.21±0.02	0.14±0.02	0.09±0.02	0.10±0.01
V-Mo	0.43±0.02	0.14±0.02	0.12±0.02	0.04±0.02	0.14±0.01

3.3. Microstructural changes on hydrogen charging

The microstructures of charged samples were analysed by TEM. All samples were imaged under the same conditions, namely close to the <100> zone axis. Fig. 7 (a) and (b) show uncharged microstructures from Ti-Mo and V-Mo steels with random dislocations with the density of $5.02\pm0.18\times10^{13}$ m^{-2} and $3.96\pm0.27\times10^{13}$ m^{-2}, respectively. After hydrogen charging, the dislocation density had increased substantially, Fig. 7 (c) and (d), with $23.9\pm1.9\times10^{13}$ m^{-2} for Ti-Mo steel and $11.6\pm3.7\times10^{13}$ m^{-2} for the V-Mo steel, as detailed in Table 4.

Fig. 8 (a) shows a bright field TEM image taken under two beam conditions of the uncharged Ti-Mo steel showing the classic lobe diffraction contrast associated with coherent precipitates. Similar images were obtained for the finer precipitates in the V-Mo steel. Fig. 8 (b) shows a bright field image of the V-Mo steel after charging, taken under the same imaging conditions as Fig. 8 (a). There has been significant changes to the image contrast on charging. It was not possible to obtain the classic lobe diffraction contrast from the precipitates after charging. In addition the size of the strain field, as shown by diffraction contrast, was much larger after charging, Fig. 8(b). To further explore the effect of charging on the strain field around the finer precipitates, high resolution imaging was undertaken. Fig. 9 show high resolution TEM (HRTEM) and associated FFT on the precipitates without and with hydrogen charging. In the

uncharged state, Fig. 9 (a-c), it is relatively straight forward to image both the precipitate and the matrix and to get an understanding of the interface between the two. This was true for both steels and was identical from grain to grain. However, on charging, it proved impossible to get a clear HRTEM image from the matrix around the precipitate in the strain field region, Fig. 9 (d-f). The images show that the distortion occurred in the strain field in the matrix, but there was no evidence of distortion in the precipitate itself (Fig. 9 (f)).

The residual stresses were measured in the uncharged and charged states using the method described in the experimental procedure. Compressive stresses were found in both alloys in the uncharged state, with similar magnitude, Table 4. The value of this stress increased on charging for both alloys, with a much more significant increase for the Ti-Mo alloy compared to the V-Mo alloy.

Table 4.

Table showing the precipitate size and number density, and the dislocation density before and after charging. The residual stress values are taken from a separate publication which was on the same materials [37]

Material	Dislocation density $[10^{13} \text{ m}^{-2}]$	Precipitate density $[\mu\text{m}^{-2}]$	Precipitate radius [nm]	Residual stress [MPa]
Ti-Mo uncharged	5.02 ±0.18	550±37.5	5.8±0.08	–343
Ti-Mo charged	23.9 ±1.9	–	–	–602
V-Mo uncharged	3.96 ±0.27	420±30.6	7.9±0.08	–347
V-Mo charged	11.6 ±3.7	–	–	–470

3.4. The effect of the hydrogen charging on the tensile behaviour

3.4.1 Tensile behaviour

Fig. 10 shows the engineering tensile stress-strain curves and corresponding work hardening rates of stress-strain curves from conventional tensile tests for the uncharged and hydrogen charged steels. The as-received Ti-Mo sample exhibited continuous yielding with a total strain to failure of 11% and UTS of 800 MPa (Fig. 10 (a)). The V-Mo steel (Fig. 10 (b)) had a lower elongation than the Ti-Mo steel, 5.8%, and also a lower UTS at 790 MPa for the V-Mo steel. Hydrogen charging resulted in a decrease in total elongation and tensile strength for both steels. The tensile properties are summarised in Table 5. The susceptibility of the Ti-Mo steel to HE was much greater than in the V-Mo steel.

Table 5.

Mechanical properties from Ti-Mo and V-Mo steels before and after hydrogen charging

Material	Yield Strength (YS by 0.2% in length, MPa)	Ultimate tensile strength (UTS, MPa)	Elongation (%)
Ti-Mo uncharged	580	800	11
Ti-Mo charged	--	643	0.6
V-Mo uncharged	413	790	5.8
V-Mo charged	420	679	3.6

The work hardening rate as a function of true strain for the two steels are shown in Fig. 10 (c) and (d). The charged Ti-Mo steel failed around the yield point so there is no information on the work hardening rate. The charged V-Mo steel exhibited lower rates of work hardening immediately after yield when compared to the uncharged samples. As straining proceeded, the

work hardening rate of the charged samples became similar to that of the uncharged samples, but failure occurred soon after.

3.4.2 The effect of the hydrogen charging on crack propagation and the deformation substructure in tensile samples tested to failure

The morphology of the tensile fracture surfaces on the two steels are shown in Fig. 11. In the absence of hydrogen, the fracture surface of both steels showed the expected microvoid coalescence typical of tensile ductile failure, Fig. 11 (a) and (b). When charged for 48h a mixed morphology fracture surface was observed with some microvoid coalescence, but otherwise the surface dominated by quasi-cleavage facets, Fig. 11 (c) and (d). The extent of microvoid coalescence was greater for the V-Mo steel than the Ti-Mo steel, which was dominated by quasi-cleavage fracture. Cross-sections of the tensile fracture surface showed that any secondary cracking seen in the plan view specimens did not extend far below the fracture surface and that there was no evidence of subcritical crack growth, Fig. A4.

The quasi-cleavage fracture was largely in the ferrite. Moreover, the morphology of the quasi-cleavage fracture allowed crack initiation sites to be identified, Fig. 12 (a) and (d). Crack initiation was found to be entirely in the ferrite with no evidence of the martensite playing a part. The initiation site often had a spherical appearance, suggesting that it was associated with a second phase particle such as MnS. EDS analysis of the crack initiation sites found no evidence of second phase particles. Multiple FIB sections were removed from the initiation sites to investigate them in more detail. In none of these were second phase particles found. Selected images are given in Fig. 12 (b) and (c) for Ti-Mo steel and (e) and (f) for V-Mo steel. The initiation sites in both steels were similar in characteristics. No evidence of second phase particles was found at any initiation site. Rather the shape of the feature arises from a dislocation wall that separates a region of low dislocation density from the surrounding

microstructure Fig. 12 (b, e). A detailed analysis of the misorientation across these boundaries was presented in [58]. It was shown that the misorientation across these boundaries was typically 15-20°, but the one shown in Fig. 12 (e) was measured as 57°. Secondary cracking was also evident, Fig. 12(f).

Figs. 13 (a) and (d) show SEM images of the same fracture surfaces as in Fig. 12, but showing regions of quasi-cleavage propagation. FIB specimens were removed from the cleavage surface away from the region of initiation. Electron diffraction from the FIB specimens show that in both cases the crack propagated broadly along a (100) cleavage plane. STEM bright field images show the microstructure below the cleavage fracture in more detail, Figs. 13 (b) and (c), for the Ti-Mo steel, and (e) and (f), for the V-Mo steel. The dislocation density in the Ti-Mo steel was comparatively low, with loose dislocation tangles pinned by precipitates, particularly the rows of interphase precipitates. Of course, the strain to failure was limited in the charged Ti-Mo steel, so a small dislocation density would be expected. In the V-Mo steel, the dislocation density was much higher below the cleavage surface than the Ti-Mo steel, comprising dislocations pinned by the precipitates forming a rudimentary cell structure.

Higher magnification images were taken of the dislocation substructures in the Ti-Mo steel below the cleavage surface. Fig. 14 gives an HRTEM image showing the distinct tilt nature of the boundary, which suggests an array of edge dislocations, which is surprising in a steel specimen.

Fig. 15 shows a subsurface crack in the Ti-Mo steel from the same FIB TEM sample taken from the charged tensile sample as shown in Figs. 12 & 13. The dislocation substructure near the crack was similar to elsewhere, namely a low dislocation density with some rudimentary cell structures. An orientation image, which use precession electron diffraction to evaluate the misorientations around the crack and specifically at the crack tip, is shown in Fig. 15 (c), which

shows that misorientation was low, except at the crack tip. Here, a subgrain boundary extended a small distance from the crack tip. There was a gradual change in lattice curvature perpendicular to this boundary, with the boundary itself having a misorientation of ~8°, Fig. 15 (d).

To observe the interaction of crack growth and interphase precipitates, FIB specimens were removed from secondary crack tips, shown in Fig. 16. Fig. 16 (a) and (b) show the crack tip in the charged Ti-Mo steel. Crack propagation was highly crystallographic. The crack edge exhibited a zigzag like crack path, with propagation predominantly along {100} planes. Interestingly, crack propagation was clearly between the rows of precipitates. The crack adopted a tortuous crack path at the atomic scale by switching from {100} to {110} planes to ensure that the overall propagation route fell in between the precipitate rows. This effect is further shown in Fig. 16 (d) and (e), which is taken from the crack wake. Thus, crack propagation was clearly affected by the strain field around the precipitates.

Although failure in hydrogen charged samples appeared to be associated with initiation in the ferrite grains, cracking was also found associated with the martensite and martensite/ferrite boundaries. Fig. 17 shows what is perhaps best described as voiding in the martensitic regions in the V-Mo steel. Fig. 17 (a) shows voiding at a ferrite/ martensite boundary (top), with voiding along the martensite lath boundary in the lower part of the image. The latter martensite region is magnified in Fig. 17 (b). There is also extensive voiding at triple junctions, as shown in Fig. 17 (c) and (d), with small cracks growing into the ferrite. Although these features were significant, we found no evidence that they played a role in the failure mechanism. It would appear that these were more ductile aspects of the damage accumulation in the samples, while failure was associated with the cleavage fracture.

3.4.3 The crack growth behaviour from notched tensile samples

To understand the effect of hydrogen on crack growth from a notch, two notched tensile samples were used, whereby failure occurred from one notch, while the other notch exhibited extensive damage, but no failure. EBSD was used to understand the crack growth behaviour from this second notch.

Fig 18 shows EBSD images from the uncharged V-Mo steel, which exhibited shear failure at 45° to the notch and microvoid coalescence far from the notch, typical of ductile failure in steel failure mode in the absence of hydrogen charging. Similar observations were found in both T-Mo and V-Mo steels.

Fig. 19 shows EBSD maps taken from the edge of the notch from the hydrogen charged Ti-Mo steel. Cracks were observed that initiated from the notch and propagated in a transgranular manner in a direction perpendicular to the tensile axis. Fig. 19 (a-c) shows one of many similar such cracks. The initiation region was difficult to study but it was clear that the crack propagated across a grain along the trace of the {100} planes. The crack was arrested at the grain boundary, with evidence of crack tip plasticity in the adjacent grain as shown by the KAM image in Fig. 19 (a). The KAM map gives a measure of the geometrically necessary dislocation (GND) distribution in the sample. Interestingly, the evidence of residual lattice curvature around the crack and crack tip was minimal. Fig. 19 (d-f) shows a crack in the middle of the specimen, equidistant between the two notches. Again, the crack was transgranular and followed the {100} trace in going from grain to grain, Fig. 19 (f). Fig. 19 (d) is a KAM map. Interestingly, the cracking does not occur in regions of the highest GND density, rather it appears to propagate in grains with minimal GND.

Fig. 20 shows the results of a similar investigation of the charged double notched V-Mo steel. Similar behaviour was observed to the Ti-Mo steel. However, secondary cracks were also

extensively observed at the phase boundary between the ferrite and martensite colonies and propagating through the martensite, Fig. 20 (d-f). The cracks also grew along the trace of the {100} planes in the ferrite, but when the crack propagated into the martensite crack growth was along the trace of the {110} planes. Surprisingly in this example (and several others), the crack was propagating parallel to the stress axis.

4.Discussion

In this study, Ti-Mo and V-Mo high strength steels have been analysed in detail before and after hydrogen charging to understand the mechanisms of hydrogen embrittlement and how changes in precipitate type effect the mechanisms. For both steels, hydrogen charging had a significant effect on the ductility of tensile samples, Fig. 10. The extent of the degradation of properties was a strong function of composition. The Ti-Mo steel suffered brittle failure around the yield point, with quasi-cleavage dominating the fracture surface. In contrast, the V-Mo steel exhibited appreciable ductility in the charged condition (~35% reduction on charging), although failure was dominated by a significant amount of quasi-cleavage fracture, with a reduction of the UTS from 790 to 697MPa. Hydrogen had an effect on the work hardening rate, with the initial work hardening less than the uncharged steel, but then the work hardening rates became similar with higher strain, up to failure of the charged sample.

4.1 Hydrogen trap density, hydrogen trapping sites and changes to microstructure from hydrogen charging

4.1.1. Hydrogen trapping

The TDS curves in Fig. 5, quantified in Tables 2 & 3, show two peaks for both steels. TDS measurements are accurate to better than ±5%, so the differences between the two steels is significant. The first peak is known to be associated with trapping at a number of different sites, namely dislocations, grain boundaries, martensite lath boundaries and at coherent precipitates [38-49]. In order to determine the origin of the low temperature peak, it was deconvoluted into

17

3 peaks, Fig. 6, with activation energies and trapped hydrogen content given in Table 3. The best fit yielded three peaks with activation energies of 18, 35 and 55kJ/mol for the Ti-Mo steel and 18, 35 and 58kJ/mol for the V-Mo steel.

There have been numerous studies into the origins of the low temperature TDS peak, with significant differences in the trap energies reported for apparently similar features [38-47]. TDS gives indirect information on trapping and is a combination of several different factors, such that interpretation is complicated. Moreover, for carbide traps, small changes in the composition of the carbide or the nature of the interface with the matrix have significant effects on the trapping behaviour.

The first deconvoluted peak had an approximate activation energy of 18mJ/mol. The low temperature peak is usually considered to be associated with dislocations. Atomistic calculations of the binding energies have been undertaken by a wide range of authors, summarised in [50]. Bombac et al. [51] have recently reported binding energy values of 27-32.8kJ/mol for quantum mechanically informed kinetic Monte Carlo simulations on edge and screw dislocations. Similarly, Kholtobina et al. [50] calculated values of 20.3, 35.7kJ/mol for screw and mixed dislocations respectively. However, experimentally estimated values of activation energy of trapping at dislocations are often slightly higher. For example, Drexler et al. [48] have investigated the trapping in deformed DP steels, thereby separating the trapping specifically associated with dislocations, reporting values of 32.3 and 36.1kJ/mol (depending on the strain). Similarly, Okano & Takagi [49] reported a value of 30.1kJ/mol associated with dislocations derived from straining ferritic, DP and martensitic steels.

In the current steels, charging was found to increase the dislocation density, which is a new observation as the vast majority of investigations did not compare the uncharged and as-charged microstructures, which will be discussed in detail in a subsequent section. The Ti-Mo

exhibited a much higher dislocation density after charging (23.9×10^{13} m^{-2}) compared to the V-Mo steel (11.6×10^{13} m^{-2}), Table 4. The hydrogen trapped in this 1st peak was much larger for the Ti-Mo steel (0.21 ± 0.02wppm) compared to the V-Mo steel (0.14 ± 0.02wppm), Table 3. These values are consistent with the much larger dislocation density in the Ti-Mo steel compared to the V-Mo steel.

The second deconvoluted peak had an estimated activation energy of 35kJ/mol for both steels, with approximately the same amount of hydrogen trapped in each. This peak is believed to be associated with boundaries, both grain boundaries and boundaries within the martensite. Atomistic calculations of the trapping at grain boundaries report wide variations in values depending on whether they are twist or tilt boundaries and particular crystallographic planes involved. Kholtobina et al. [50] recently reported binding energy values of 45 and 55kJ/mol for twist and tilt boundaries respectively. A wide range of binding energies are reported in the literature (summarised by Kholtobina et al. [50]) in the range 25-80kJ/mol depending on the specific boundary type. There are many experimental values reported, for example, Depover & Verbeken [43] measured activation energy values of 25, 28 and 30 mJ/mol for as quenched martensitic steels, with the trap sites in this case corresponding primarily to martensite lath boundaries but will have also included grain boundaries. Choo and Lee [52] reported activation energy for grain boundaries of 23.34kJ/mol while Berstein [53] reported a value of 33kJ/mol.

There was a difference in the grain size and in the volume fraction of martensite between the two steels. The Ti-Mo steel had the finest grain size (9.7μm) compared to the V-Mo steel (19.1μm) and so had approximately 4x larger grain boundary area, which would lead to greater trapping at these sites and therefore a larger TDS peak. However, the V-Mo contained a greater fraction of martensite (~20%) compared to the Ti-Mo (~5%), which would have contributed to the hydrogen trapped in the second peak. The differences in grain size and martensite lath

boundary content between the two steels will have offset each other in the size of peak 2 leading to the similar amount of hydrogen trapped in peak 2, Table 3.

The third peak obtained by deconvolution of the low temperature peak is believed to be associated with reversibly trapped hydrogen at fine coherent precipitates. The measured activation energy of this peak of ~55kJ/mol for the Ti-Mo steel and 58kJ/mol for the V-Mo steel is consistent with values in the literature. Depover and Verbeken [43] report activation energies of 52 kJ/mol, associated with the carbide/matrix interface in a quench and tempered Fe-C-Mo martensitic steel, which is similar to the 58kJ/mol reported here. Similarly, Drexler et al. [38] report binding energies of 32kJ/mol for a coherent vanadium carbide/matrix interface, and 58kJ/mol for carbon vacancies at the carbide/matrix (001) interface. For Ti bearing steels, much more data exists, with Wei et al. [56] reporting 46kJ/mol for nanosized TiC in a martensitic matrix for the 'low carbon' variant and 58kJ/mol in the 'high carbon' variant. The latter value is the same as reported here and is in-line with values from Drexler et al. [38] who report binding energies of 58kJ/mol for carbon vacancies at the TiC/matrix (001).

In the current work the carbides were not formed through a quench and temper, as investigated in the literature, rather through interphase precipitation. Interphase precipitation resulted in a bimodal size distribution of the precipitates (Fig.3), with finer coherent carbides and slightly coarser semi-coherent particles (i.e. coherent TiC and semicoherent Ti_2C for the Ti-Mo steel and coherent VC and semicoherent V_4C_3 for the V-Mo steel). Peak 3 was therefore believed to be associated with the finer, coherent TiC in the Ti-Mo steel and VC in the V-Mo steel. This is consistent with Takahashi et al. [54] who used atom probe to show no trapping of deuterium at fine coherent VC (believed to be a reversible trap), but trapping occurred at semi-coherent V_4C_3, which was believed to be an irreversible trap. Similarly, Echeverri Restrepo et al. [55] used DFT calculations to show only weak trapping at coherent VC/ferrite interfaces.

The second high temperature peak, Fig. 5, has been seen by numerous authors [40, 47, 56-60]. The second peak has been universally assigned to irreversible trapping of hydrogen at carbides, including titanium, molybdenum and niobium based carbides. In the current work, the activation energy, Ea, associated with the high temperature peak was measured as 73.8kJ/mol for the Ti-Mo steel and 66.9 kJ/mol for the V-Mo steel. Drexler et al. [39] reported binding energy of 76kJ/mol for trapping at carbon vacancies at the precipitate/matrix (011) interface for TiC and 73.4kJ/mol for the same interface with V_4C_3. Similarly, Yoo et al. [47] report an activation energy of 83.4kJ/mol for TiC precipitates in a 'low carbon' tempered martensitic steel. Wei et al. [56], report that the the E_a of TiC in martensite can be in the range of 46–86.9 kJ/mol, with the variation arising from differences in interfacial coherency. Thus, the current values are in-line with those reported in the literature, with any differences associated with the specific structure of the interface between precipitate and matrix. In any event, trap binding energies of these values are generally considered to be irreversible traps and not likely to contribute to hydrogen embrittlement [43].

The hydrogen content in the high temperature peak was ~1.4x higher in the V-Mo steel compared to the Ti-Mo steel. Interpretation of the high temperature peak is complicated by having a bimodal carbide size distribution in both the Ti-Mo and V-Mo steels. In each case, the finer, coherent, precipitates led to the simulated peak 3 of the low temperature peak, while the coarser semi-coherent precipitates led to the high temperature peak. The proportion of coarser particles was greater for the V-Mo steel compared to the Ti-Mo steel, Fig. 4, consistent with the greater proportion of semi-coherent precipitates in the V-Mo steel.

Theoretical studies have indicated that the trapping of hydrogen at precipitates is complicated [55,59,61,62,63,64]. Di Stephano et al., [62] provided DFT calculations on a comprehensive set of interfaces between ferrite and TiC. Trapping at semi-coherent interfaces was found to be moderate with more efficient trapping at carbon vacancies in the interior of the TiC. However,

such traps are difficult to populate unless there are percolating networks of C vacancies, requiring a sub-stoichiometric carbide. Kawakami and Matsumiya [61] have performed detailed *ab initio* calculations on trapping in the strain field, at the carbide/matrix interface and within the precipitate for Fe-TiC and Fe-V_4C_3 steels. This showed a significant difference in behaviour between the TiC and V_4C_3. They concluded that for coherent TiC precipitates, the main trap site is the Fe/TiC interface. In contrast, their calculations concluded that the main trap site for V_4C_3 was at carbon vacancies within the precipitate, which reflects the differences in vacancy concentration between TiC and V_4C_3. Similarly, more recent DFT calculations by Echeverri Restrepo et al. [55] show that the perfect coherent interface traps H only weakly, but much stronger trapping can be expected at C vacancies, both at the interface and in the bulk of the VC.

The work of Kawakami and Matsumiya [61] is consistent the recent 3D atom probe studies of Chen et al. [65] on deuterium charging of a steel that was nearly identical to that used in the current work. They carefully analysed the location of the deuterium and clearly demonstrated that it was trapped within the V_4C_3 precipitates [65]. In contrast, Takahashi et al. [54] found no trapping of deuterium at VC precipitates in an underaged steel, but believed that deuterium was trapped at misfit dislocations at the ferrite/V_4C_3 interface in a peak aged sample. In a similar study on relatively large TiC plate-like precipitates in a ferritic steel, Takahashi et al. [66] also found deuterium at the precipitate/matrix interface. The difference in trap site, whether at the precipitate/matrix interface or within the precipitate is important as it could affect the liberation of hydrogen from the trap sites in the vicinity of a crack. The differences in the reversible trapping behaviour between the Ti based carbides and the V based carbides, with around twice as much hydrogen reversibly trapped in the Ti-Mo steel compared to the V-Mo steel will be one reason for the much greater embrittlement of the Ti-Mo steel compared to the V-Mo steel. The reasons for the differences in the steels is considered further in the subsequent sections.

4.1.2 Changes in microstructure on charging

The charging clearly modified the strain field around the precipitates in both steels, Figs. 8, 9. Diffraction contrast TEM images, Fig. 8 (b) showed that the strain field around the precipitates was greatly increased by hydrogen charging. HRTEM images indicated that changes occurred in the matrix adjacent to the precipitate, with changes in the precipitate itself too small to detect, Fig. 9 (d-f)). In addition, the residual stress in the samples measured by XRD increased substantially on charging (Table 4), which is consistent with this enlargement of the strain field (this specific point is discussed later). This is the first observation of hydrogen significantly changing the strain field around precipitates. As discussed later, the strain field around the precipitates played a significant role in determining the crack propagation at the atomic scale.

The hydrogen charging increased the dislocation density in both steels quite substantially, Table 4. The increase was far greater for the Ti-Mo steel, around 5x, compared to the V-Mo steel, around 3x. Not only was the dislocation density increased but also the dislocation structures were different. After hydrogen charging dislocations were generally pinned by precipitates, and in several places arranged in tangles forming rudimentary cells structures (Fig. 7 (c) and (d)). In contrast, in the uncharged state random dislocation distributions were observed (Fig. 7 (a) and (b)). Similar increases in dislocation density have been observed on charging in the literature [67,68]. Barnoush et al. [68] used classical dislocation theory to model homogeneous dislocation nucleation and showed that hydrogen reduces the activation energy for homogeneous dislocation nucleation (HDN). Thus, they demonstrated that hydrogen reduces the required stress for HDN by a reduction in the shear modulus, dislocation line energy and stacking fault energy. Moreover, they showed that the hydrogen induced activation energy for HDN could be used to rank the sensitivity to hydrogen embrittlement of various metal alloys. The residual stresses could reach levels sufficient for triggering dislocation activity [69]. In the current work, it is probable that the increase in dislocation density on charging was associated

with the increase in strain in the strain field around precipitates. As quantified in Section 4.2.3, this factor was much greater for the Ti-Mo steel than the V-Mo steel. On the other hand, the formation of dislocation cells is regarded as a sign of a reduction in the interaction energy of dislocations, also due to hydrogen. Of course, dislocations pinned by precipitates in this way will provide a local source of hydrogen, with hydrogen accumulations being key to failure.

4.2 Observations from the tensile specimens strained to failure

4.2.1 Tensile work hardening

For the V-Mo steel, the work hardening rate immediately after yield was lower for the hydrogen charged specimen compared to the hydrogen free, Fig. 10, although work hardening rates became similar at higher strains. While in many steels, the work hardening rate is the same for charged and uncharged specimens, there have been several observations of different work hardening rate after charging [70-73], although there was little attempt to explain the observations. A reduction in flow stress could be explained by cracking and/or voiding in the sample during tensile deformation. However, we undertook detailed investigations and confirmed that there was no cracking in the samples, except at the final failure site. While there was some voiding at subgrain walls, Fig. 17, this was too small to account for the differences in flow stress and was only prevalent at higher strains when work hardening rates were similar in charged and uncharged samples. Therefore, the lower flow stress is more likely to be associated with the higher density of more mobile dislocations in the charged specimen, before normal work hardening processes set in. Indeed, calculations for the same steels investigated here, presented in detail elsewhere [37], indicate that hydrogen leads to an increase in dislocation mobility of 14 to 17 times.

4.2.2 Dislocation substructure and crack initiation

For the uncharged case, both steels exhibited classic ductile failure with microvoid coalescence, as expected, Fig. 11 (a) and (b). Hydrogen charging led to a complete change in the fracture

surface, with extensive quasi-cleavage and secondary cracking, particularly for the Ti-Mo steel, Fig. 11 (c) and (d). Plan view images of the fracture surface allowed crack initiation sites to be identified, Fig. 12. These were found to be entirely in ferrite, with no evidence of crack initiation in the martensite. This finding is in contrast to that of Koyama et al. [24], who examined a DP steel and found crack initiation was predominantly at the martensite/martensite boundaries and that hydrogen reduced the crack-arresting ability of the ferrite. However, the martensite comprised 55vol% of the microstructure in Koyama et al.'s work, while in the current work, the amount of martensite was relatively small, being ~20% in the V-Mo steel and only 5% in the Ti-Mo steel. Moreover, the extensive precipitation in the ferrite clearly gave significant changes to the mechanical properties and dissolution of hydrogen of the ferrite compared to a conventional DP steel.

FIB samples were removed from the fracture surface, both from the initiation sites and propagation regions (the latter discussed in the next section). Hydrogen charging promoted a higher dislocation density prior to testing (Table 4) and that was also reflected in the failed specimens. The crack initiation sites are shown in detail in Fig. 12. The shape of the crack initiation, with its "fish eye" appearance suggested that second phase particles, such as MnS or carbides would be the source of initiation. However, despite extensive investigation, no second phase particles were seen. Instead, a unique effect was observed, whereby cracks were initiated at low-energy dislocation walls. It is well established that hydrogen charging leads to an increase in dislocation mobility in steels [74]. Calculations for the same steels investigated here, presented in detail elsewhere [37], indicate that hydrogen leads to an increase in dislocation mobility of 14 to 17 times. This results in the accelerated dislocation cell and subgrain formation observed in this work. The dislocation walls at the crack initiation sites exhibited a pronounced misorientation between a region of low dislocation density (light contrast in Figs. 12 (b), (e)) and the surrounding region. Detailed modelling [37] showed that the crack initiated

as a result of this strain partitioning. In forming low energy dislocation structures, the hydrogen is released to produce substantial local hydrogen concentrations [75-77], originating cracks. Propagation after initiation was by quasi-cleavage, discussed in the next section.

The observation of crack initiation at low energy dislocation walls could be taken as consistent with the HELP mechanism. HELP is explained in terms of a hydrogen shielding model in which the presence of hydrogen atmospheres around dislocations and elastic obstacles decreases the interaction energy between them [20]. The decreased barrier to dislocation motion and the increased mobility leads to localised deformation, with reduced dislocation separation at dislocation pile-ups which results in the nucleation of microcracks. While the current observations show similarities to the HELP mechanism, the observation of cracking associated strain partitioning at low energy dislocation structures is unique.

4.2.3 Crack propagation

Fig.13 gives a general view of the fracture surface in a region that was clearly associated with crack propagation, but within 50 μm of where the crack was known to initiate. FIB samples were removed from these regions to examine the dislocation structures, the crack propagation and the crack tip associated with secondary cracks. The crack propagation is clearly strongly influenced by the precipitate structures, with ridges on the surface of the crack associated with the coarser precipitate rows, Fig. 16. High resolution plan views of the cleavage surface made it look like potential surface voids, but the detailed cross-sectional TEM of the cleavage surface clearly showed that the surface topography was associated with small changes in crack propagation in the vicinity of precipitates, but that the crack remained crystallographic at all times.

A detailed analysis was made of these crack surfaces and where possible, crack tips associated with secondary cracking. In the uncharged case, the cracking had no specific crystallographic

nature, with the features better described as voids. In contrast, in the hydrogen charged samples, crack propagation was clearly shown to be crystallographic, with growth along {100} and {110} planes, Fig. 16. Interestingly, the cracks grew specifically in between the precipitate rows. The change from {100} to {110} and back again to {100} allowed the crack to avoid the compressive strain field associated with the precipitates. Thus, the strain field around the precipitates, which was enlarged by hydrogen charging, had a key role in determining the quasi-cleavage crack propagation.

The dislocation density associated with the crack tip of a propagating crack was low, as shown in Figs. 15, 16 and 19. Indeed, no evidence was found of dislocation activity at the crack tip that would be consistent with a HELP type mechanism. In addition, the dislocation density observed in FIB specimens taken from the crack surface, away from the crack tip (i.e. the crack wake), also exhibited low dislocation density. This is in contrast to the observations of Nagao et al. [80] who observed intense plasticity below the crack wake surface in a quenched and tempered medium carbon martensitic steel. At first sight, the multiple observation of low dislocation density in the current work might be interpreted as being consistent with a HEDE mechanism [78-80]. However, Song and Curtin [26] have demonstrated that the HEDE mechanism is physically unlikely. They showed that a ductile to brittle transition occurs by the suppression of dislocation emission at the crack tip due to the aggregation of hydrogen driven by the crack tip stress fields. The absence of dislocation emission at the crack tip, as observed in the current work, removes the crack blunting mechanism. Cleavage then becomes the only available energy relieving mechanism. This mechanism requires hydrogen in the lattice around the crack tip. The TEM observations, Fig. 13, showed that dislocations induced on charging were trapped by the precipitate structures in the vicinity of the propagating crack. These would have provided a plentiful source of weakly trapped hydrogen. Nevertheless, the current observations could be taken as being consistent with a HEDE mechanism.

4.2.4 Comparison of the two steels and the role of residual stress

The significant difference in embrittlement between the Ti-Mo and the V-Mo steels has to be explained. The Ti-Mo repeatedly exhibited failure at yield, while the V-Mo steels retained significant ductility. There were several differences between the two steels on charging. TDS showed that the Ti-Mo steel trapped more hydrogen in low temperature, reversible, trapping sites than the V-Mo steel. The Ti-Mo steel had a higher grain boundary area (~4x the V-Mo steel) which resulted in ~2x the amount of hydrogen being trapped reversibly at these sites compared to the V-Mo steel. Charging promoted a much higher dislocation density in the Ti-Mo steel (23.9×10^{13} m^{-2}) compared to the V-Mo steel (11.6×10^{13} m^{-2}). Hydrogen was also reversibly trapped at coherent precipitates, with much more hydrogen trapped at TiC than at VC, Table 3. Moreover, the hydrogen charging increased the strain field around the precipitates.

The combination of these factors led to a significant increase in residual stress on charging, with the increase far greater for the Ti-Mo steel compared to the V-Mo steel, Table 4. The residual stresses are believed to play a role in crack propagation and the limited ductility of Ti-Mo grade. The residual stress values reported in Table 4 are made up of three microstructural contributions:

(1) A Taylor effect ($\sigma_T = -M\alpha\mu b\sqrt{\rho}$), due the dense dislocation forests compared to the un-deformed states. $M = 3$ stands for the Taylor factor due to the crystal orientation, $\alpha = 0.25$ is a constant, $\mu = 80$ GPa is the shear modulus, $b = 0.25$ nm is the magnitude of the Burgers vector and ρ is the dislocation density. σ_T can be computed from the experimental dislocation density values from Table 4.

(2) Precipitation, $\sigma_P = -E\epsilon_i V_i^{1/3}$ resulting from the matrix strain as the dense precipitates display a dissimilar lattice parameter to the matrix, leading to a strain ϵ_i. By accounting for the

28

i precipitate radius and number density shown in Table 4, it becomes possible to estimate the *i* precipitate volume fraction $V_i^{1/3}$.

(3) The stress due to the expansion of precipitates by trapping hydrogen, $\sigma_H = -kEV_i^{1/3}$. In this case, the expansion due to hydrogen is taken as $k = 0.005$.

With above considerations, the following contributions to residual stress are calculated:

Table 6.

Contribution to residual stress estimated from microstructural observations. All values expressed in MPa.

Material	σ_T	σ_P	σ_H	Total residual stress
Ti-Mo uncharged	−106	−204	–	−310
Ti-Mo charged	−232	−204	−230	−666
V-Mo uncharged	−94	−42	–	−136
V-Mo charged	−162	−42	−274	−477

Referring to Table 6, most total residual stress values are very close to those experimentally obtained (Table 4). The UTS – YS is the stress amount available for plastic deformation. Values of UTS and YS are given in Table 5. For the Ti-Mo steel, the UTS – YS is 220 MPa, lower than the stress due to the expansion of precipitates by trapping hydrogen, σ_H, of 230 MPa, Table 6; whereas for the V-Mo steel, the UTS – YS is 377 MPa, well above the 274 MPa residual stress developed upon charging. The saturation of trapped hydrogen by precipitates adds a significant extra element to the residual stress, which inhibits plastic deformation. This is consistent with the crack growth observations; when a crack forms in the Ti-Mo steel,

plasticity at the crack tip is limited as the extra strain energy required around the crack tip is already taken by dislocations, precipitates and their expansion due to hydrogen. V-Mo instead displays a limited amount of lattice straining which allows the crack propagation along {100} planes in the ferrite.

4.3 The crack propagation and growth mechanism from notched samples after hydrogen charging

To further understand the mechanism of early stage crack propagation, double notched samples were used whereby failure occurred from one notch, but the other exhibited some limited crack propagation.

4.3.1 The crack propagation mechanism in the ferrite Ti-Mo steel

Fig. 19 gives EBSD maps of regions containing cracks, both at the notch and in the centre of the sample, remote from the notch. Transgranular cracks along the {100} planes were dominant, with no cracking at the grain boundaries. The cracks were arrested at grain boundaries (e.g. Fig. 19 (c,f)) or propagated through the next grain with a different orientation to the stress axis, but still following the trace of the {100} plane, (Fig. 19 (c,f)).

KAM maps give an indication of the lattice curvature. The KAM map of the crack propagating from the notch, Fig. 19 (a) exhibited very little lattice curvature in the vicinity of the crack. The exception is a small amount of plasticity in the grain adjacent to the crack tip, but in this case the crack appears to have arrested at the grain boundary. The situation was more complex at secondary cracks in the centre of the specimen, Fig. 19 (d-f). The KAM map showed regions of extensive lattice curvature, but these tended not to be associated with cracking. The flanks of the cracks showed virtually no evidence of plasticity. However, the crack tips were associated with regions of high lattice curvature, but again, the curvature appears to be in the grain adjacent to the crack tip, with the crack, at least temporarily, arrested at the grain boundary. The overall conclusion is that there was no evidence of enhanced crack tip plasticity,

rather the opposite. Therefore, these results are consistent with tensile tests, which suggests that enhanced dislocation mobility and dislocation pile-ups (i.e. HELP mechanisms) were not important in crack propagation. Rather the observations of propagation are consistent with the model of Song and Curtin [26] or indeed HEDE.

4.3.2 The crack propagation mechanism in V-Mo steels

The cracks in the charged V-Mo steel are shown in Fig. 20. Similar behaviour was observed to the Ti-Mo steel. However, secondary cracks were also extensively observed at the phase boundary between the ferrite and martensite colonies and propagating through the martensite, Fig. 20 (d-f). The cracks also grew along the trace of the {100} planes in the ferrite, but when the crack propagated into the martensite crack growth was along the trace of the {110} planes, Fig. 20 (d). The crack growth in the martensite was not only along the lath martensite lath boundaries, but also propagation occurred transverse across the lath boundaries. The preferential propagation of cracks at the ferrite/martensite boundary and through the martensite itself, compared to propagation in the ferrite, is consistent with the observations of Koyama et al. [24]. This is a result of hydrogen preferentially diffusing to the inter-phase grain boundaries and the lath boundaries. Koyama et al. [24] take this as evidence of a HEDE mechanism operating both within the martensite and also at the martensite/ferrite boundaries, although they also found that HELP was also important. As discussed earlier with respect to the tensile results, this result can also be taken as consistent with the model of Song and Curtin, who demonstrate that embrittlement results from the suppression of dislocation emission from the crack tip and so crack tip blunting does not occur.

Surprisingly, the crack propagated parallel to the stress axis in several cases, which is similar to observations of Koyama et al. [24]. In the vicinity of the notch, Fig. 20 (a-c) this might be a result of the complex stress system. However, this phenomenon was also observed in the middle

of the specimen, Fig. 20 (d-f). It clearly shows the preferential crack path along lath boundaries that is preferential to propagation perpendicular to the stress axis through the martensite.

5 Conclusions

In the present work, the hydrogen embrittlement has been analysed through the mechanical properties, TDS curves and microstructures such as dislocation activity and cracks in the Ti-Mo and V-Mo steels.

1. Thermal desorption spectroscopy showed two distinct peaks for both steels, with the low temperature peak associated with trapping at grain boundaries, phase boundaries, dislocations and coherent precipitates, and a high temperature peak associated with trapping at semi-coherent precipitates. The Ti-Mo steel exhibited a larger low temperature peak, which was associated with the finer grain size but mainly the large increase in dislocation density on charging (which was much greater than in the V-Mo steel). The V-Mo steel exhibited a larger high temperature peak, which was believed to be associated with hydrogen irreversibly trapped within the precipitates. In contrast, in the Ti-Mo steel, the hydrogen was believed to be irreversibly trapped at the precipitate/matrix interface. The increase in dislocation density and the increase in strain field around the precipitates led to a large increase in residual stress on charging, with the extent far larger for the Ti-Mo steel than the V-Mo steel.

2. Hydrogen charging resulted in severe embrittlement in the Ti-Mo steel, with failure occurring at yield in a tensile test. Hydrogen reduced the ductility in the V-Mo steel, with quasi-cleavage replacing ductile failure, but the extent of hydrogen embrittlement was much less than in the Ti-Mo steel, despite a similar microstructure.

3. Crack initiation in charged tensile samples appears to have occurred from voiding at the dislocation cell boundaries associated with strain partitioning, consistent with a HELP type mechanism. However, within a few microns, crack propagation becomes crystallographic, i.e.

quasi-cleavage with the crack following the {100} trace, with little evidence of dislocation plasticity at the crack tip. The crack tip changes from one plane to another at the nm scale as it avoids the compressive strain field around precipitates. This gives a roughness to the crack surface, which might be incorrectly interpreted as local plasticity, but is in fact crystallographic propagation with very limited plasticity. While such observation might be taken as consistent with a HEDE type mechanism, it is more consistent with the model of Song and Curtin, whereby dislocation emission is suppressed from the crack tip, with crack propagation aided by a continuous supply of hydrogen to the crack tip.

4. Similar observations were found for the double notched specimen in the Ti-Mo steel. However, in the V-Mo steel, much more extensive crack propagation was observed at the ferrite/martensite boundaries and through the martensite colonies. These represent easier crack paths than the ferrite to the extent that cracks would preferentially propagate here away from the tensile stress rather than following a direction dictated by the principal tensile stress. Again, crack propagation was associated with minimum plasticity and was believed to be consistent with the model of Song and Curtin.

5. Hydrogen saturation at trapping species may result in an increase in residual stress. This can limit ductility and inhibit plastic deformation as observed in the Ti-Mo alloy. Such embrittlement occurs when the residual stress developed upon trapping exceeds the plasticity range available for deformation, which is dictated by the difference between the ultimate tensile stress and the yield stress in the hydrogen-free condition.

Author contributions
P.G: Experimental, analysis, writing, experimental design, editing; A.T.: Experimental on TDS, analysis; J.N.: Experimental on TEM orientation imaging; F.Y.: Experimental on tensile test; B.W.: analysis, experimental design on EBSD; P.R.: analysis on residual stress; W.M.R.: experimental design, analysis, writing, editing.

References

[1].Y. Takahashi, M. Tanaka, K. Higashida, H. Noguchi, Hydrogen-induced slip localization around a quasi-brittle fatigue crack observed by high-voltage electron microscopy, Scr. Mater., 61(2009) 145-148.

[2].S. Wang, M.L. Martin, P. Sofronis, S. Ohnuki, N. Hashimoto, I.M. Robertson, Hydrogen-induced intergranular failure of iron, Acta Mater., 69(2014) 275-282.

[3].M. Martin, P. Sofronis, I. Robertson, T. Awane, Y. Murakami, A microstructural based understanding of hydrogen-enhanced fatigue of stainless steels, Int. J. Fatigue, 57(2013) 28-36.

[4].M.L. Martin, B.P. Somerday, R.O. Ritchie, P. Sofronis, I.M. Robertson, Hydrogen-induced intergranular failure in nickel revisited, Acta Mater., 60(2012) 2739-2745.

[5].Y. Takahashi, J. Sakamoto, M. Tanaka, K. Higashida, H. Noguchi, Effect of hydrogen on dislocation structures around a mixed-mode fatigue crack tip in a single-crystalline iron-silicon alloy, Scr.Mater., 64(2011) 721-724.

[6].Y. Takahashi, M. Tanaka, K. Higashida, K. Yamaguchi, H. Noguchi, An intrinsic effect of hydrogen on cyclic slip deformation around a {110} fatigue crack in Fe-3.2 wt.% Si alloy, Acta Mater., 58(2010) 1972-1981.

[7].G. Lovicu, M. Barloscio, M. Bottazzi, F.D. Aiuto, M. De Sanctis, A. Dimatteo, C. Federici, S. Maggi, C. Santus, R. Valentini, L.L. Lazzarino, Hydrogen embrittlement of automotive advanced high-strength steels, Metall Mater Trans A, 43(2012), 4075-4087.

[8].X. Zhu, W. Li, H. Zhao, L. Wang, X. Jin, Hydrogen trapping sites and hydrogen-induced cracking in high strength quenching & partitioning (Q & P) treated steel, Int. J. Hydrogen Energy., 39 (2014) 13031-13040.

[9].T. Michler, J. Naumann, B.M.W. Ag, Microstructural aspects upon hydrogen environment embrittlement of various bcc steels, Int. J. Hydrogen Energy. 35 (2009) 821-832.

[10].D.G. Enos, J.R. Scully, A Critical-Strain Criterion for Hydrogen Embrittlement of Cold-Drawn , Metal. Mater. Tran. A 33(2002) 1151-1166.

[11].M.R. Louthan, G.R. Caskey, J.A. Donovan, D.E. Rawl Jr., Hydrogen embrittlement of metals embrittlement of metals by hydrogen, Wasserstoffversprodung in Metallen, 10(1972) 357-368.

[12]. K. Knarbakk, Hydrogen Induced stress cracking of Inconel 718 under cathodic polarization-effects of hydrogen on the initiation and propagation of cracks, Doctoral dissertation, NTNU, 2015.

[13]. J. Hyun, Hydrogen Embrittlement in TRIP and TWIP Steels, Doctoral dissertation, Pohang Unviersity of Science and Technology, 2012.

[14]. J. Venezuela, Q. Zhou, Q. Liu, M. Zhang, A. Atrens, Influence of hydrogen on the mechanical and fracture properties of some martensitic advanced high strength steels in simulated service conditions, Corros. Sci. 111 (2016) 602–624.

[15].N. Eliaz, A. Shachar, B. Tal, D. Eliezer, Characteristics of hydrogen embrittlement, stress corrosion cracking and tempered martensite embrittlement in high-strength steels, Eng. Fail. Anal. 9 (2002) 167-184.

[16].T. Neeraj, R. Srinivasan, J. Li, Hydrogen embrittlement of ferritic steels: Observations on deformation microstructure, nanoscale dimples and failure by nanovoiding, Acta Mater. 60 (2012) 5160-5171.

[17].F. Wan, Q. Zhan, Y. Long, S. Yang, G. Zhang, Y. Du, The behavior of vacancy-type dislocation loops under electron irradiation in iron, J. Nucl. Mater. 455 (2014) 253-257.

[18].Y. Murakami, T. Kanezaki, Y. Mine, Hydrogen Embrittlement mechanism in fatigue of austenitic stainless steels, Metal. Mater. Tran. A, 39A(2008) 1327-1339.

[19].C.D. Beachem, A new model for hydrogen-assisted cracking (hydrogen "embrittlement"), Metall. Mater. Trans.: B, 3(1972), 441-455.

[20]. H.K. Birnbaum, P. Sofronis, Hydrogen-enhanced localized plasticity—a mechanism for hydrogen-related fracture. Mater Sci Eng A 176(1) (1994) 191–202.

[21].S.M. Meyers, M.I. Baskes, H.K. Birnbaum, J.W. Corbett, G.G. Deleo, S.K. Estricher, E.E. Haller, P. Jena, N.M. Johnson, R. Kircheim, S.J. Pearton, M.J. Stavola, Hydrogen interactions with defects in crystalline solids, Rev. Mod. Phys. 64 (1992), 559.

[22].E. Sirois, P. Sofronis, H.K. Birnbaum, in: S. M. Bruemmer et al. (eds.), Fundamental Aspects of Stress Corrosion Cracking, The Minerals, Metals and Materials Society, New York, 1992, pp. 173.

[23].H.K. Birnbaum, in N. Moody and A. W. Thompson (eds.), Hydrogen Effects on Materials Behaviour; The Minerals, Metals and Materials Society, New York, 1990, pp. 639.

[24].M. Koyama, C.C. Tasan, E. Akiyama, K. Tsuzaki, D. Raabe, Hydrogen-assisted decohesion and localized plasticity in dual-phase steel, Acta Mater., 70 (2014) 174-187.

[25].A. Tehranchi, X. Zhou, W.A. Curtin, A decohesion pathway for hydrogen embrittlement in nickel: Mechanism and quantitative prediction, Acta Mater., 185(2020) 98-109.

[26].J. Song, W.A. Curtin, Atomic mechanism and prediction of hydrogen embrittlement in iron, Nat. Mater. 12(2013) 145-151.

[27].E. Herms, J.M. Olive, M. Puiggali, Hydrogen embrittlement of 316L type stainless steel, Mater. Sci. Eng. A 272(1999) 279-283.

[28].G. Wang, Y. Yan, J.X. Li, J.Y. Huang, L,J. Qiao, A.A. Volinsky, Microstructure effect on hydrogen-induced cracking in TM210 maraging steel, Mater. Sci. Eng. A. 586 (2013) 142-148.

[29].A. Laureys, T. Depover, R. Petrov, K. Verbeken, Microstructural characterization of hydrogen induced cracking in TRIP-assisted steel by EBSD, Mater. Charact. 112 (2016) 169-179.

[30].J. Han, J.H. Nam, Y.K. Lee, The mechanism of hydrogen embrittlement in intercritically annealed medium Mn TRIP steel, Acta Mater. 113 (2016) 1-10.

[31].S.M. Sun, J.L. Gu, N.P. Chen, The influence of hydrogen on the sub-structure of the martensite and ferrite dual-phase steel, Scri. Metal. 23(1989) 1735-1737.

[32].M.E. Hilley, Ed., Residual Stress Measurement by X-ray Diffraction, SAE J784a, Society of Automotive Engineers, Warrendale, PA, 1971, p 20.

[33].P. Gong, X.G. Liu, A. Rijkenberg, W.M. Rainforth, The effect of molybdenum on interphase precipitation and microstructures in microalloyed steels containing titanium and vanadium, Acta Mater., 161(2018) 374-387.

[34].H.E. Kissinger, Reaction kinetics in differential thermal analysis, Anal. Chem. 29 (1957)1702-1706.

[35].S.M. Lee and J.Y. Lee, The effect of the interface character of TiC particles on hydrogen trapping in steel, Acta Metall., 35(11) (1987) 2695-2700.

[36].T. Depover, K. Verbeken, The detrimental effect of hydrogen at dislocations on the hydrogen embrittlement susceptibility of Fe-C-X alloys: An experimental proof of the HELP mechanism, Intl. J Hydrogen Energy, 43 (2018) 3050-3061.

[37].P. Gong, J. Nutter, P.E.J. Rivera-Diaz-Del-Castillo, W.M. Rainforth, Hydrogen embrittlement through the formation of low energy dislocation nanostructures in nanoprecipitation-strengthened steels, Science Advances, 6 (2020) eabb6152.

[38].A. Drexler, T. Depover, K. Verbeken, W. Ecker, Model-based interpretation of thermal desorption spectra of Fe-C-Ti alloys, Journal of Alloys and Compounds 789 (2019) 647-657.

[39].A. Drexler, T. Depover, S. Leitner, K. Verbeken, W. Ecker, Microstructural based hydrogen diffusion and trapping models applied to Fe-C-X alloys, Journal of Alloys and Compounds 826 (2020) 154057.

[40].Il-J. Park, S. Y. Jo, M. Kang, S-M. Lee, Y-K. Lee, The effect of Ti precipitates on hydrogen embrittlement of Fe–18Mn–0.6C–2Al–xTi twinning-induced plasticity steel, Corrosion Science, 89 (2014) 38-45.

[41].H.J. Kim, S.H. Jeon, W.S. Yang, B.G. Yoo, Y.D. Chung, H.-Y. Ha, H.-Y. Chung, Effects of titanium content on hydrogen embrittlement susceptibility of hot-stamped boron steels, J. Alloys Compd. 735 (2018) 2067–2080.

[42].T.Depover, K.Verbeken, Hydrogen trapping and hydrogen induced mechanical degradation in lab cast Fe-C-Cr alloys, Materials Science & Engineering A669 (2016) 134–149.

[43].T.Depover, K.Verbeken Evaluation of the effect of V_4C_3 precipitates on the hydrogen induced mechanical degradation in Fe-C-V alloys, Materials Science & Engineering A675 (2016) 299–313.

[44].D. Pérez Escobar, T. Depover, E. Wallaert, L. Duprez, M. Verhaege, K. Verbeken, Thermal desorption spectroscopy study of the interaction between hydrogen and different microstructural constituents in lab cast Fe–C alloys, Corrosion Science 65 (2012) 199–208.

[45].T.Depover, K.Verbeken, The effect of TiC on the hydrogen induced ductility loss and trappingbehavior of Fe-C-Ti alloys, Corrosion Science, 112 (2016) 308-326.

[46].T. Depover, E. Van den Eeckhout, K. Verbeken The hydrogen trapping ability of TiC and V_4C_3 by thermal desorption spectroscopy and permeation experiments, Procedia Structural Integrity 13 (2018) 1414–1420.

[47].J. Yoo, M. C. Jo, M. C. Jo, S. Kim, J. Oh, J. Bian, S. S. Sohn, S. Lee, Effects of Ti alloying on resistance to hydrogen embrittlement in (Nb+Mo)-alloyed ultra-high-strength hot-stamping steels, Materials Science and Engineering A, 791 (2020) 139763.

[48].A. Drexler, C. Bergmann, G. Manke, V. Kokotin, K. Mraczek, M. Pohl, W. Ecke, On the local evaluation of the hydrogen susceptibility of cold-formed and heat treated advanced high strength steel (AHSS) sheet, Materials Science & Engineering A 800 (2021) 14027.

[49].H. Okano & S. Takagi, Identification of Hydrogen Trapping Sites in a Strained Ferritic-Martensitic Dual-Phase Steel, ISIJ International, Vol. 59 (2019), No. 10, pp. 1828–1837.

[50].A.S. Kholtobina, R. Pippan, L. Romaner, D. Scheiber, W. Ecker, V.I. Razumovskiy, Hydrogen trapping in bcc iron, Materials 13 (2020) 2288.

[51].D. Bombac , I. H. Katzarov, D. L. Pashov, A. T. Paxton, Theoretical evaluation of the role of crystal defects on local equilibrium and effective diffusivity of hydrogen in iron, Materials Science And Technology, 33[13]2017 1505-1514

[52].W.Y. Choo, J.Y. Lee, Thermal analysis of trapped hydrogen in pure iron. Met. Trans. A. 13 1982, 135–140.

[53].I.M. Bernstein, The effect of hydrogen on the deformation of iron, Scr. Metall., 8 1974 343–349.

[54].J. Takahashi, K. Kawakami, T. Tarui, Direct observation of hydrogen-trapping sites in vanadium carbide precipitation steel by atom probe tomography, Scripta Materialia, 67 (2012) 213–216.

[55]. S. Echeverri Restrepo, D. Di Stefano, M. Mrovec, A. T. Paxton, Density functional theory calculations of iron -vanadium carbide interfaces and the effect of hydrogen, Intl J Hydrogen Energy, 45 2020 2382-2389.

[56].F.G. Wei, T. Hara, K. Tsuzaki, Precise determination of the activation energy for desorption of hydrogen in two Ti-added steels by a single thermal-desorption spectrum, Metall. & Mater. Trans., 35B (2004) 587-597.

[57].F.G. Wei, T. Hara, T. Tsuchia, K. Tsuzaki, Hydrogen trapping in quenched and tempered 0.42C-0.30Ti steel containing bimodally dispersed TiC particles, ISIJ International, 43 (2003) 539-547.

[58].F.G. Wei, K. Tsuzaki, Quantitative analysis of hydrogen trapping of TiC particles in steel, Metal. Trans. 37A (2006) 331-353.

[59].G.M. Pressouyre, I.M. Bernstein, A kinetic trapping model for hydrogen-induced cracking, Acta Metall., 27 (1979), 89-100.

[60].H. Mohrbacher and T. Senuma, Alloy optimisation for reducing delayed fracture sensitivity of 2000MPa press hardening steel, Metals 10 (2020) 853

[61].K. Kawakami, T. Matsumiya, Numerical analysis of hydrogen trap state by TiC and V_4C_3 in bcc- Fe, ISIJ Intl., 52(2012) 1693-1697.

[62].D. Di Stefano, R. Nazarov, T. Hickel, J. Neugebauer, M. Mrovec, C. Elsässer, First-principles investigation of hydrogen interaction with TiC precipitates in α-Fe, Physical Review B 93, 184108 (2016)

[63].Y. Itsumi, D.E. Ellis, Electronic bonding characteristics of hydrogen in bcc iron : Part II Grain boundaries, J. Mater. Res., 11(9)(1996) 2214-2219.

[64]. S. Yamasaki, H.K.D.H. Bhadeshia, M_4C_3 precipitation in Fe-C-Mo-V steels and relationship to hydrogen trapping, Proc. Math. Phys. Eng. Sci., 462(2006) 2315-2330.

[65]. Y.S. Chen, D. Haley, S.SA. Gerstl, A.J. London, F. Sweeney, R.A. Wepf, W.M. Rainforth, P.AJ. Bagot, M.P. Moody, Direct obesrvation of individual hydrogen atoms at trapping sites in a ferritic steel, Science, 355(2017) 1196-1199.

[66]. J. Takahashi, K. Kawakami, Y. Kobayashi, T. Tarui, The first direct observation of hydrogen trapping sites in TiC precipitation-hardening steel through atom probe tomography, Scripta Materialia, 63 (2010) 261-264.

[67]. M. Deutges, H.P. Barth, Y.Z. Chen, C. Borchers, R. Kirchheim, Hydrogen diffusivities as a measure of relative dislocation densities in palladium and increase of the density by plastic deformation in the presence of dissolved hydrogen, Acta Mater., 82(2015) 266-274.

[68]. A. Barnoush, M. Zamanzade and H. Vehoff, Direct observation of hydrogen-enhanced plasticity in super duplex stainless steel by means of in situ electrochemical methods, Scripta Materialia 62 (2010) 242–245.

[69]. A. Barnoush, H. Vehoff, Recent developments in the study of hydrogen embrittlement: Hydrogen effect on dislocation nucleation, Acta Mater., 58 (2010) 5274-5285.

[70]. M. Koyama, S. M. Taheri-Mousavi, H. Yan, J. Kim, B. C. Cameron, S. S. Moeini-Ardakani, J. Li, C. C. Tasan, Origin of micrometer-scale dislocation motion during hydrogen desorption, Sci. Adv. 2020; 6: eaaz1187.

[71].H. Luo, Z. Li, D. Raabe, Hydrogen enhances strength and ductility of an equiatomic high-entropy alloy, Scientific Reports, 7 (2017) 9892 1-7.

[72]. D. Rudomilova, T. Prosek, G. Luckeneder, Techniques for investigation of hydrogen embrittlement of advanced high strength steels, Corros. Rev. 36 (2018) 413-434.

[73]. Y. Yagodzinskyy, T. Saukkonen, E. Andronova, L. Rissanen, H.. Hänninen, Effect of Hydrogen on Plastic Strain Localization in Single Crystals of Nickel and Austenitic Stainless Steel in Effects of Hydrogen on Materials: Proceedings of the 2008 International Hydrogen Conference, September 7-10, 2008, Jackson Lake Lodge, Grand Teton National Park, Wyoming, USA. 123 (ASM International) 97-104.

[74]. P. Gong, I. Katzarov, J. Nutter, A.T. Paxton, W.M, Rainforth, The influence of hydrogen on plasticity in pure iron-theory and experiment, Sci. Rep., 10209(2020) 1-14.

[75]. H. Wakita, Y.J. Nakamura, I. Kita, N. Fujll, K. Notsu, Hydrogen release: new indicator of fault activity, Sci., 210(1980) 188-190.

[76].C.F. Dong, Z.Y. Liu, X.G. Li, Y.F. Cheng, Effects of hydrogen-charging on the susceptibility of X100 pipeline steel to hydrogen-induced cracking, Int. J. Hydrog. Energy, 34(2009) 9879-9884.

[77].M. Nagumo, M. Nakamura, K. Takai, Hydrogen thermal desorption relevant to delayed-fracture susceptibility of high-strength steels, Matel. Mater. Tran. A 32A(2001) 339-347.

[78]. R.A. Oriani, Hydrogen embrittlement of steels, Ann. Rev. Mater. Sci., 8(1978) 327-357.

[79].H. Asahi, D. Hirakami, S. Yamasaki, Hydrogen trapping behavior in vanadium-added Steel, ISIJ Int., 43(2003) 527-533.

[80].A. Nagao, C.D. Smith, M. Dadfarnia, P. Sofronis, I.M. Robertson, The role of hydrogen in hydrogen embrittlement fracture of lath martensitic steel, Acta Mater., 60 (2012) 5182-5189.
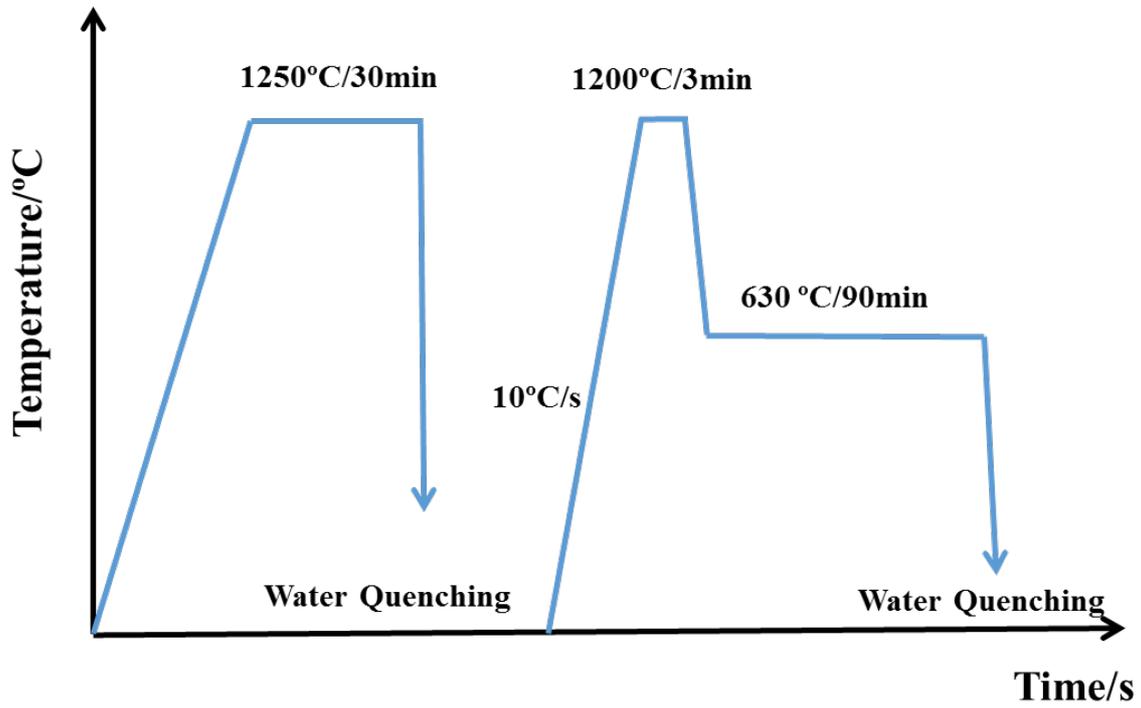
Fig. 1. Schematic of the thermomechanical cycles used on Ti-Mo and V-Mo steels.
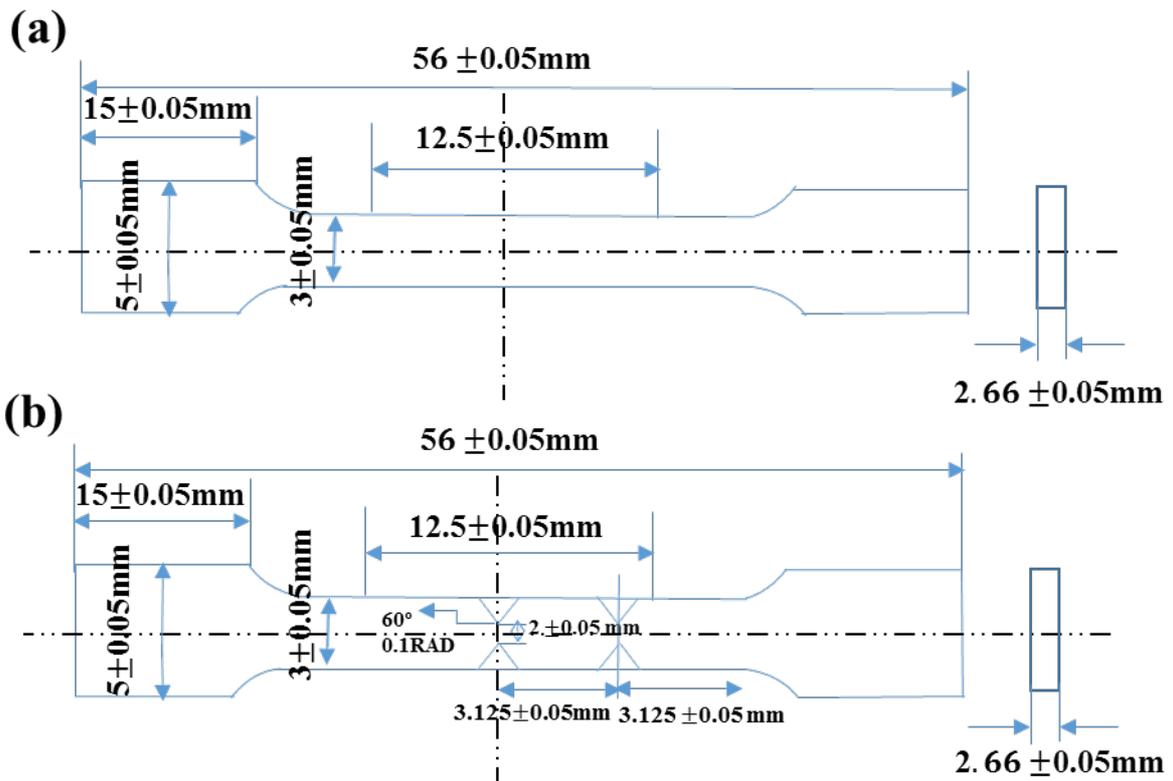
Fig. 2 Tensile sample geometry (lengths in mm): (a) without notch; (b) with two notches.
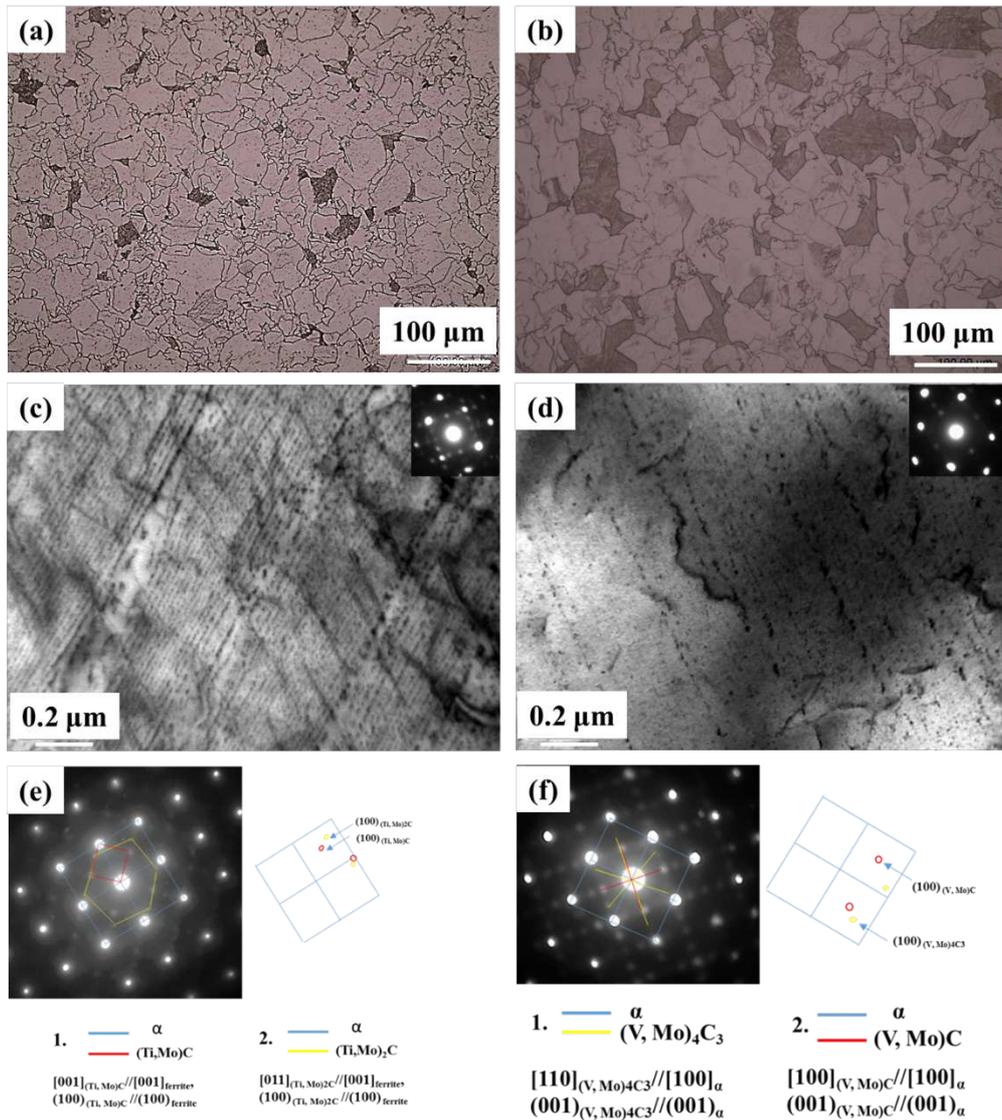
Fig. 3. (a, b) optical micrographs taken from specimens isothermally treated at 630°C for 90min for the (a) Ti-Mo steel; (b) V-Mo steel; (c, d), bright field TEM micrographs showing the interphase precipitation from thin foil samples in (c) Ti-Mo steel; (d) V-Mo steel; (e) $[001]_\alpha$ diffraction pattern and schematic showing the presence of (Ti,Mo)C (finer) and (Ti,Mo)$_2$C (coarser); (f) $[001]_\alpha$ diffraction pattern and schematic showing the presence of (V,Mo)C (finer) and (V,Mo)$_4$C$_3$ (coarser).
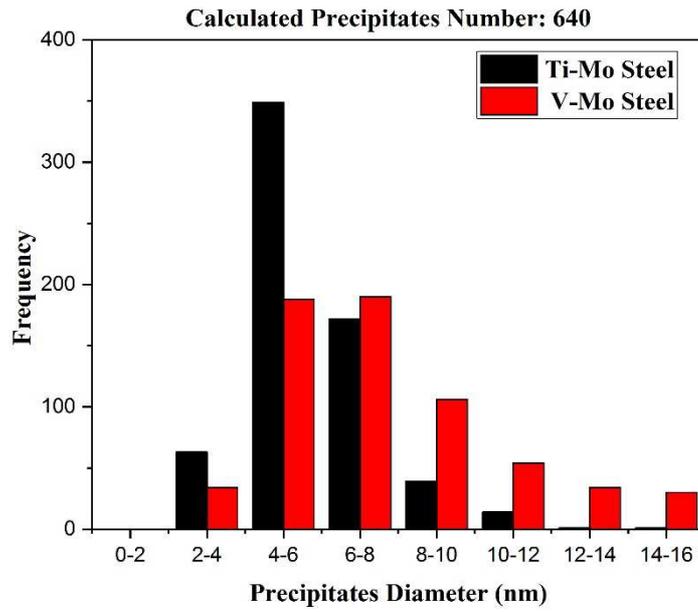
Fig. 4. Precipitate size distributions for both steels
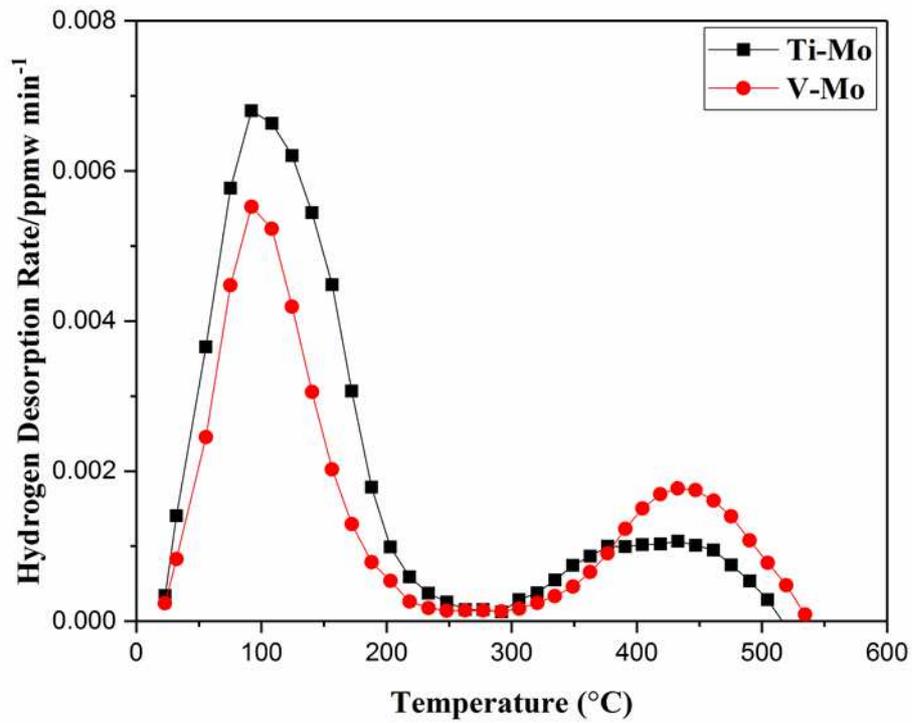
Fig. 5. Thermal desorption analysis spectra on Ti-Mo and V-Mo steels after hydrogen charging at a heating rate of 100 °Ch⁻¹.
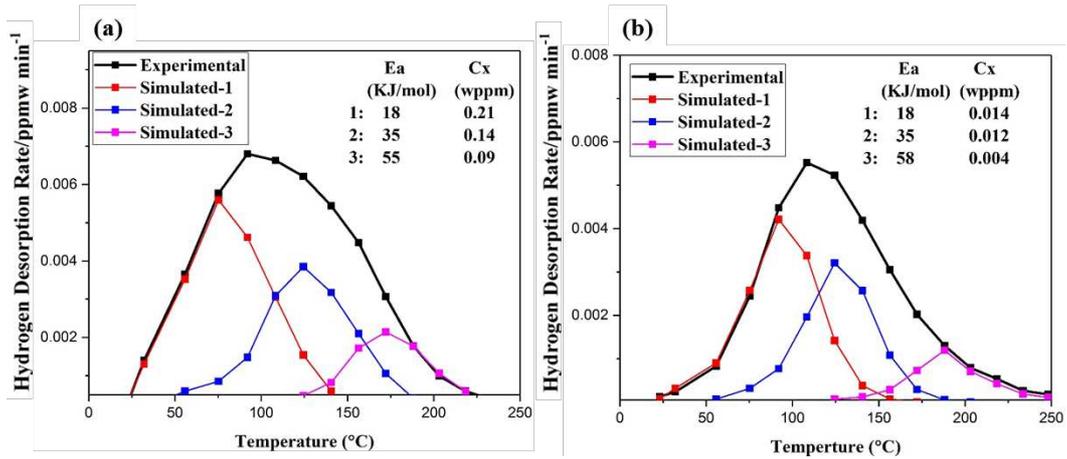
Fig. 6. Deconvolution of the low temperature TDA peak for: (a) Ti-Mo steel and (b) V-Mo steel.
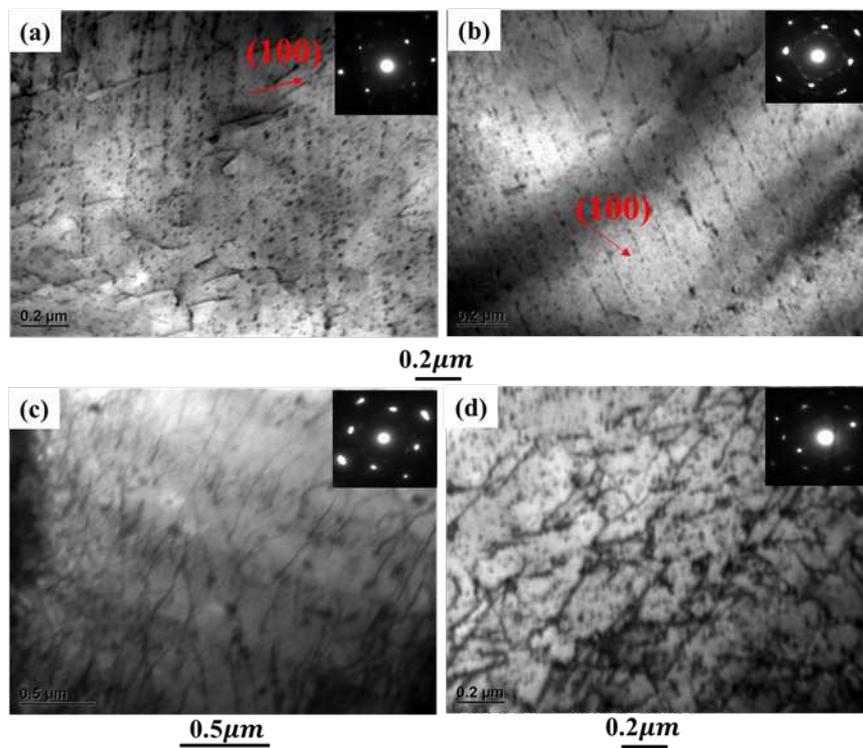
Fig. 7. TEM bright field micrographs showing uncharged and charged microstructures, with no strain application, (a,c) in the Ti-Mo steel and (b,d) in V-Mo steel. (a,b) a low density of randomly distributed dislocations from uncharged bulk samples; (c,d) a significant increase in the dislocation density from charged bulk samples.
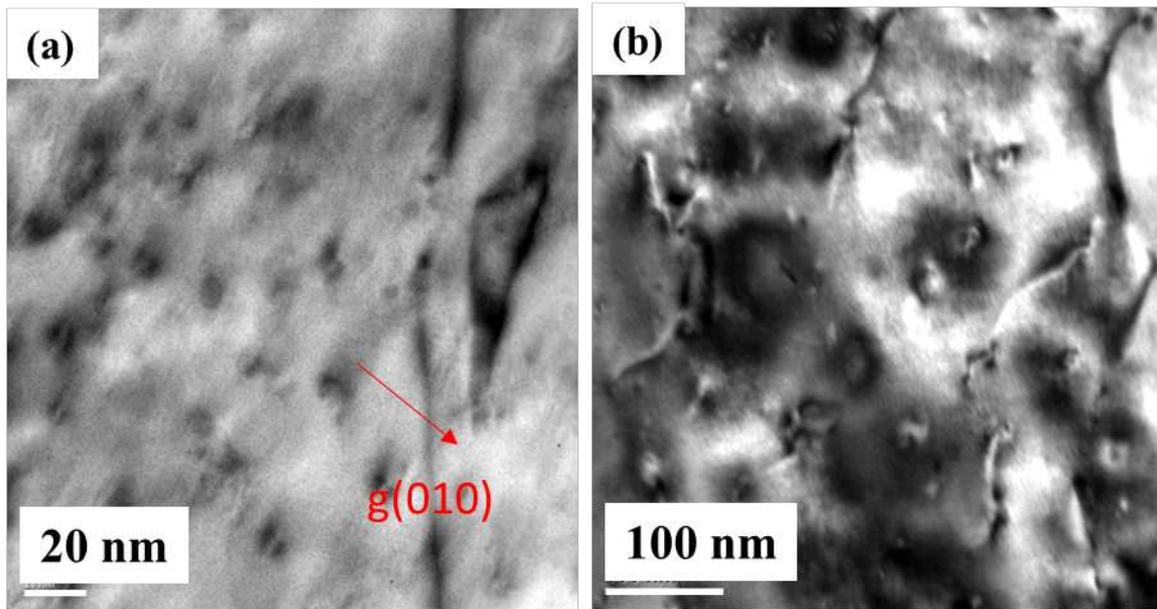
Fig. 8. Bright field TEM images formed under 2-beam conditions (g=(010)) showing the strain field around the precipitates in the Ti-Mo steel. a) Uncharged state, where the classic lobe contrast from coherent precipitates is observed. b) Charged state, where the diffraction contrast from the strain field is seen to greatly increase, and the classic lobe constrast is lost.
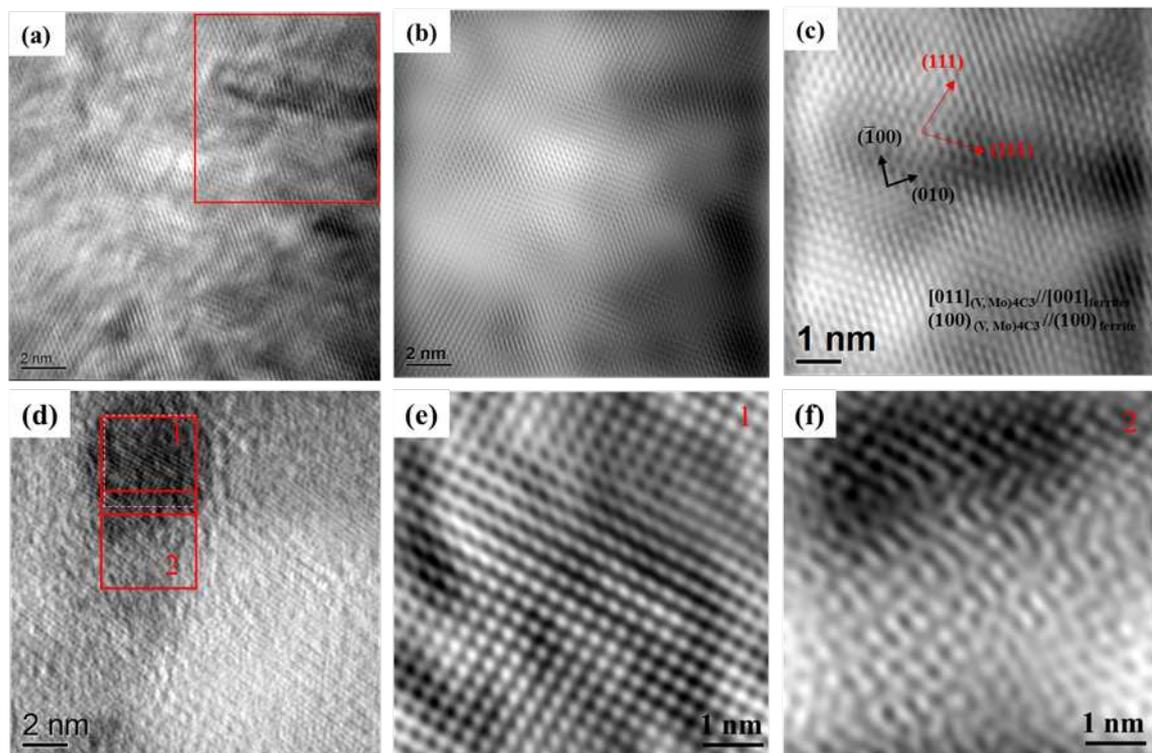
Fig. 9. HRTEM images of a coherent carbide from uncharged (a,b,c) and charged (d, e, f) Ti-Mo steel. (a) HRTEM of the carbide and (b) associated FTT filtered image of the same area as (a); (c) FTT filtered image on the interface between carbide and ferrite matrix from red square in (a); (d) HRTEM on carbide in the charged sample; (e) FTT filtered image of the carbide from red square of 1 in (d); (f) FTT filtered image on the interface between carbide and ferrite matrix from red square of 2 in (d).
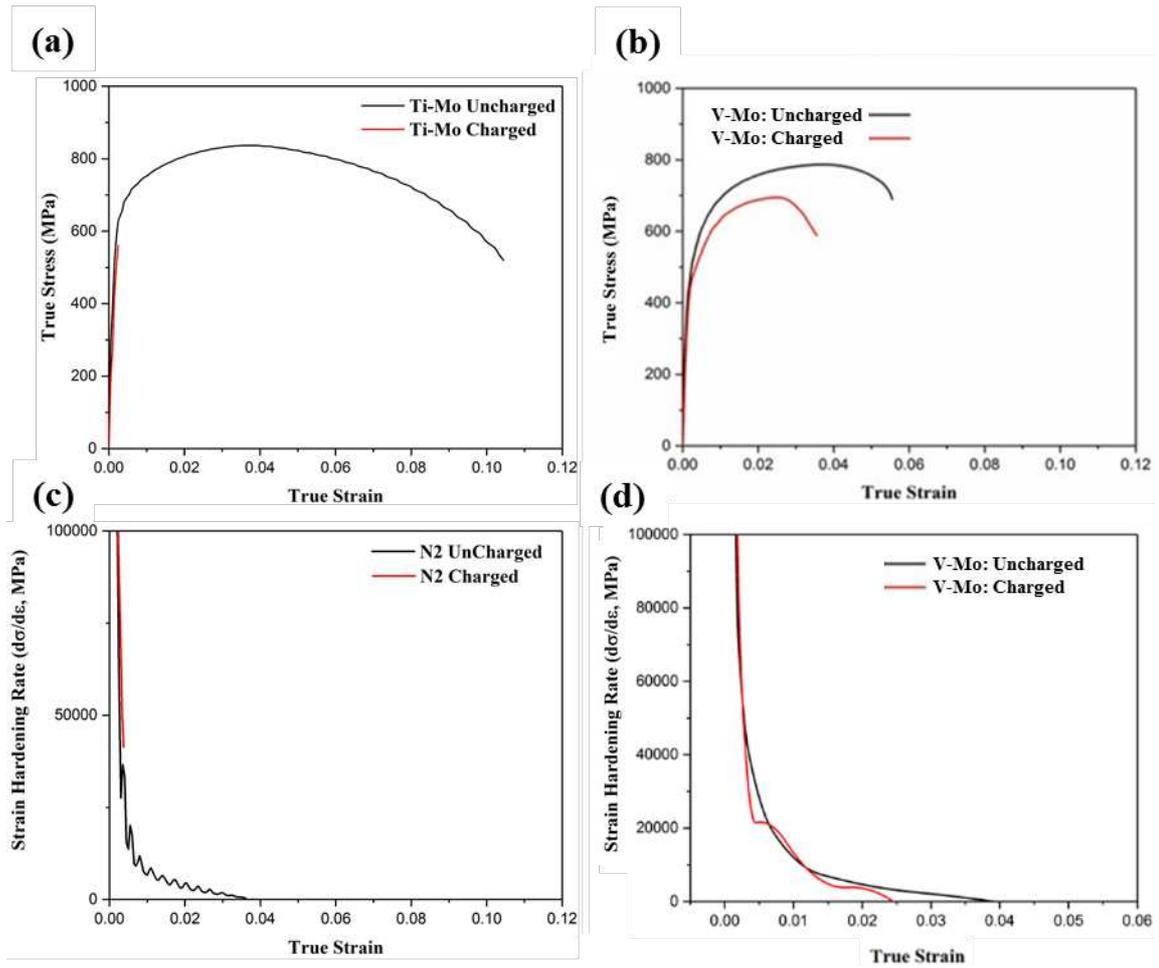
Fig. 10. (a,b) Engineering tensile stress-strain curves and the (c,d) work hardening rate curves of the (a) and (c) Ti-Mo steel, (b) and (d) V-Mo steel, with uncharged and charged tensile samples tested to failure at room temperature. Slow strain-rate tensile (SSRT) tests were performed immediately after charging (within 5 min).
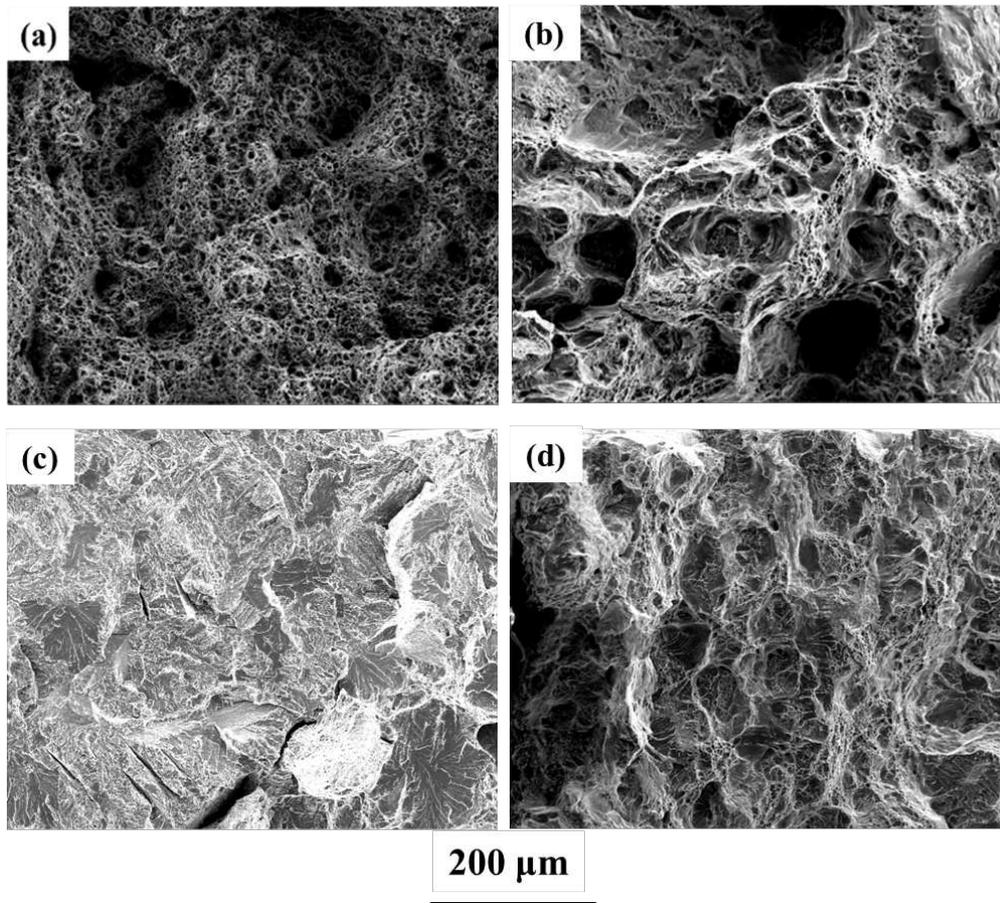
Fig. 11. SEM images of fracture surface of specimens without and with hydrogen charging, (a, c) for the Ti-Mo steel; (b, d) V-Mo steel. (a, b) hydrogen uncharged and (c, d) hydrogen charged.
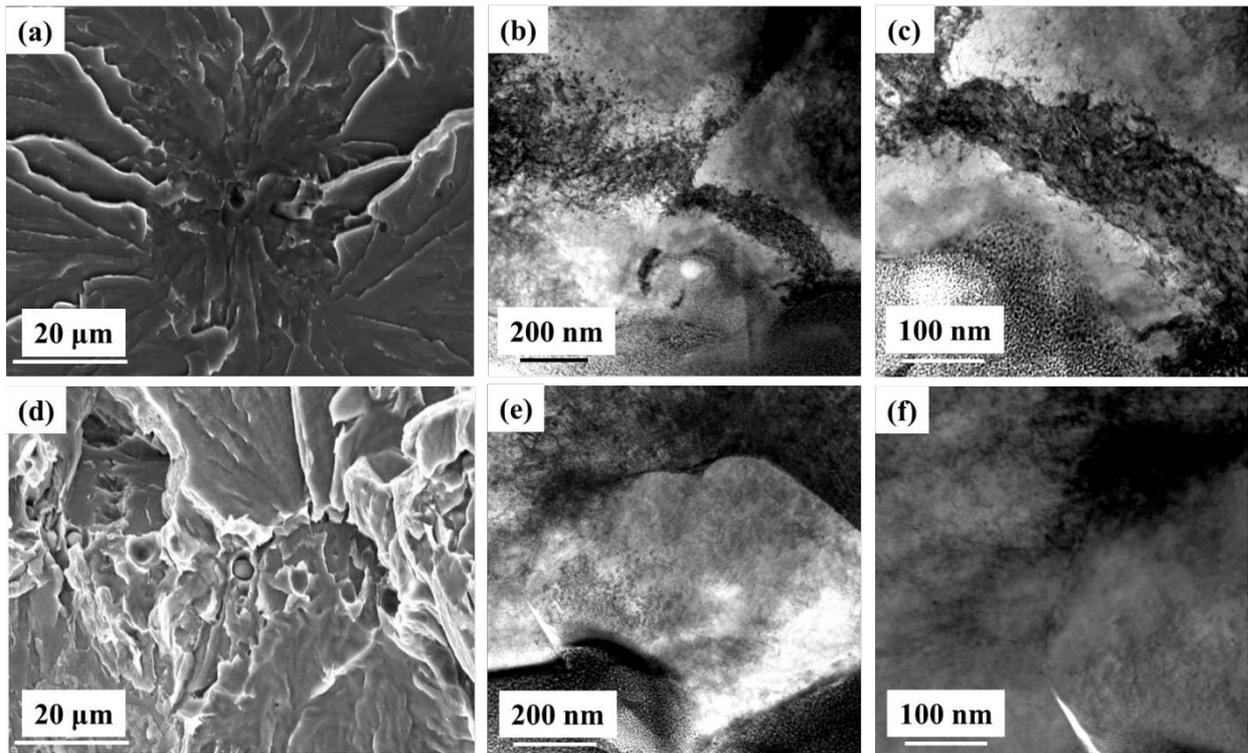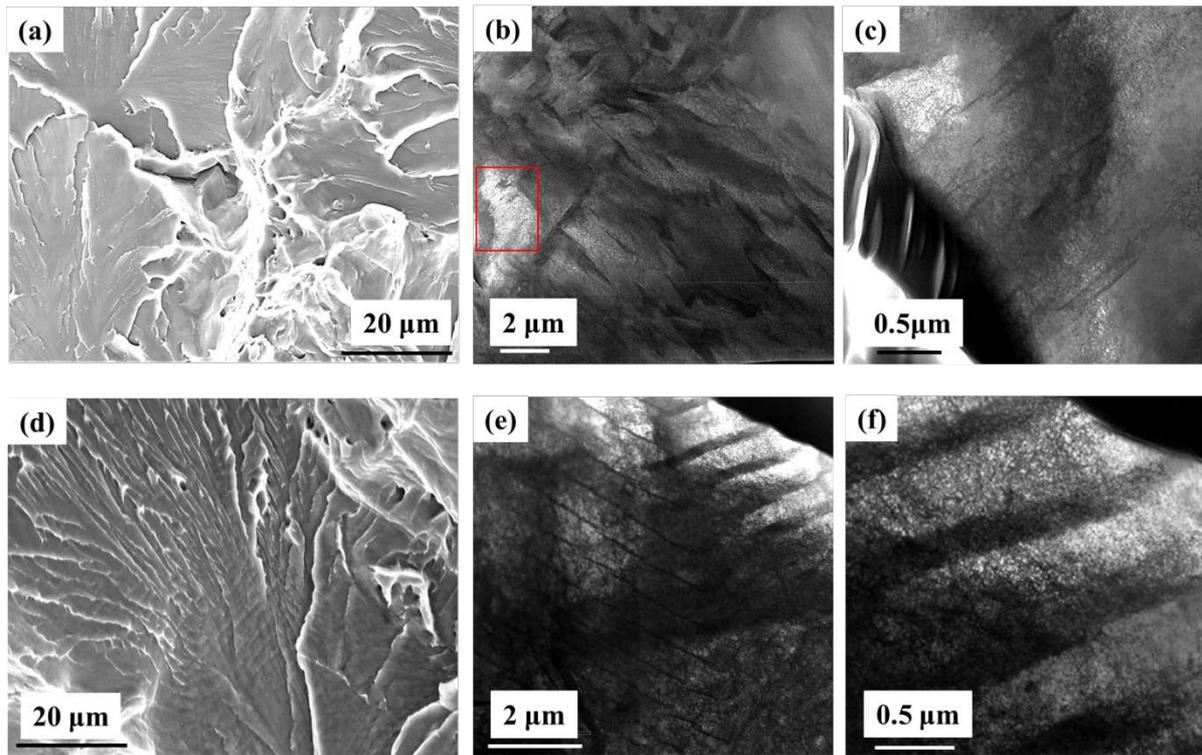
Fig. 12. Microstructures from the tensile cleavage fracture surface in charged samples for (a-c) Ti-Mo steel and (d-f) V-Mo steel. (a, d) SEM showing the cleavage fracture surface with crack initiation site, from which the FIB samples were prepared; (b) STEM image of the crack initiation site in the Ti-Mo steel, with (c) higher magnification image of the crack initiation site showing a boundary between the high dislocation density region and adjacent low dislocation density region. (e) STEM image of the initiation site in the V-Mo steel, showing a sharp boundary between the high dislocation density region and adjacent low dislocation density region; (f) STEM image showing a crack at the initiation site.

Fig. 13. Microstructures from the tensile cleavage fracture surface in charged samples for (a-c) Ti-Mo steel and (d-f) V-Mo steel. (a, d) SEM showing the quasi cleavage fracture surface from which the FIB sample was prepared; (b) STEM image from the FIB section showing the crack propagation; (c) STEM image near the fracture surface, showing the dislocation structures with dislocations pinned by precipitates. (e) STEM image from the FIB section of the quasi-cleavage crack propagation regions, with higher magnification in (f), both showing that ridges seen in the SEM image (d) were associated with rows of the larger V_4C_3 precipitates.
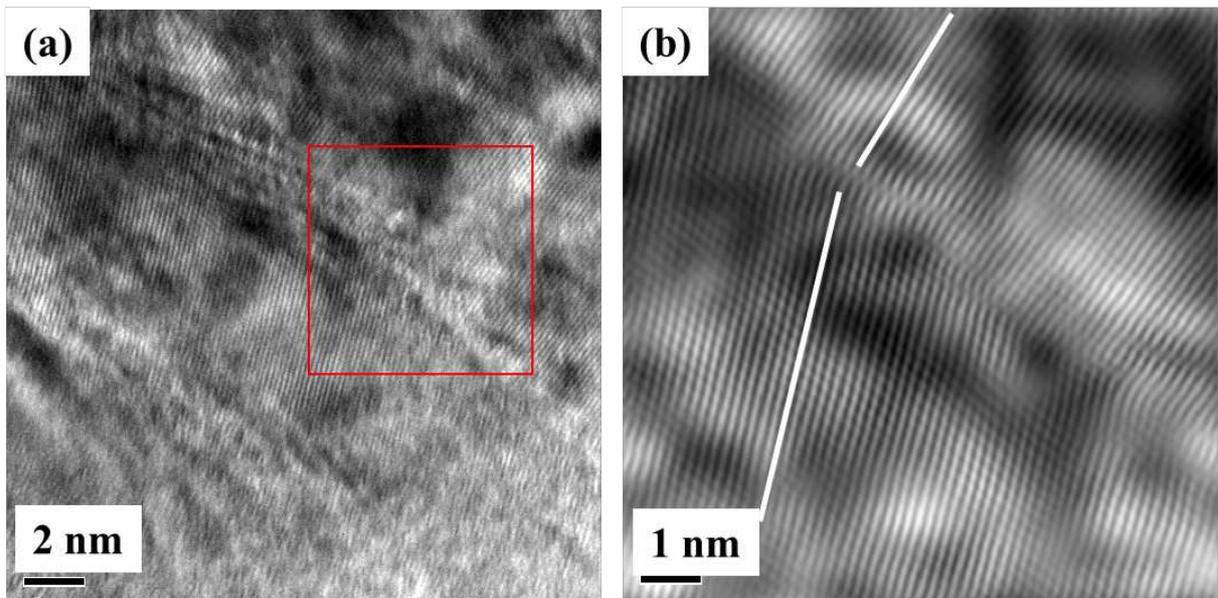
Fig. 14. HRTEM micrographs from FIB specimen below the cleavage surface of the tensile sample fracture surface of the Ti-Mo steel, showing a tilt boundary.
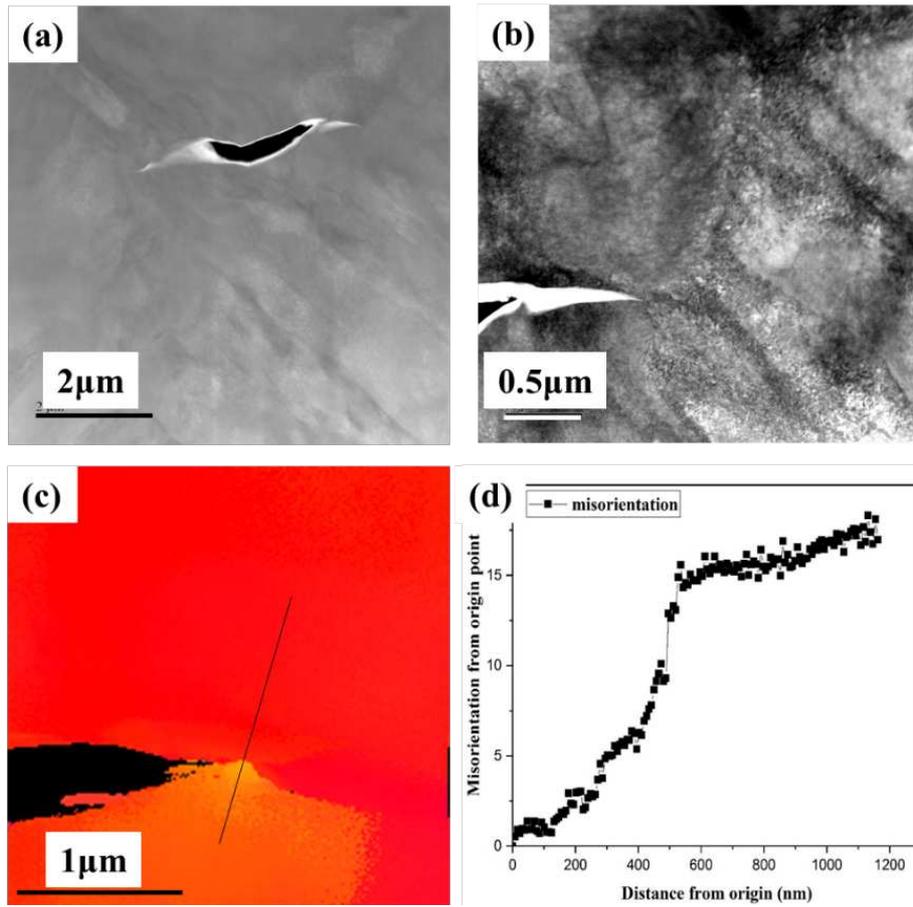
Fig. 15. Micrographs of secondary crack in Ti-Mo steel after hydrogen charged from FIB lift out TEM sample on tensile fractures showing: (a) STEM HAADF (high-angle annular dark field) low magnification image showing the position of the secondary crack; (b) STEM HAADF higher magnification images on one side of the crack tip showing the dislocation structure around the crack; (c) Orientation image from crack tip; (d) Misorientation along the line drawn in (c).
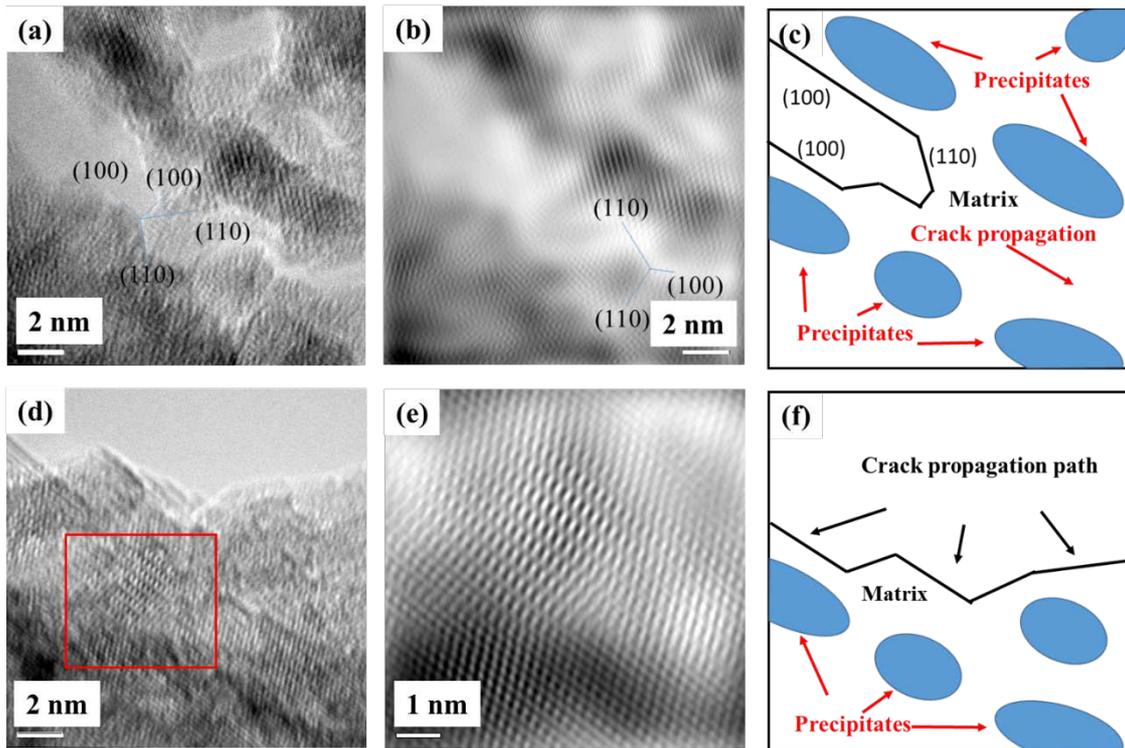
Fig. 16. Secondary crack growth in the charged tensile fracture in the Ti-Mo steel: (a) HRTEM image taken from a secondary crack and (b) FFT filtered image from (a), showing crack propagation along (100) and (110); (c) schematic from (a); (d) HRTEM image showing the crack wake, showing the atomic level propagation of the crack. Precipitates are marked below the surface. The growing crack avoids the precipitates; (e) FFT filtered image from the region marked in (d) showing a precipitate local to the crack; (f) schematic from (d).
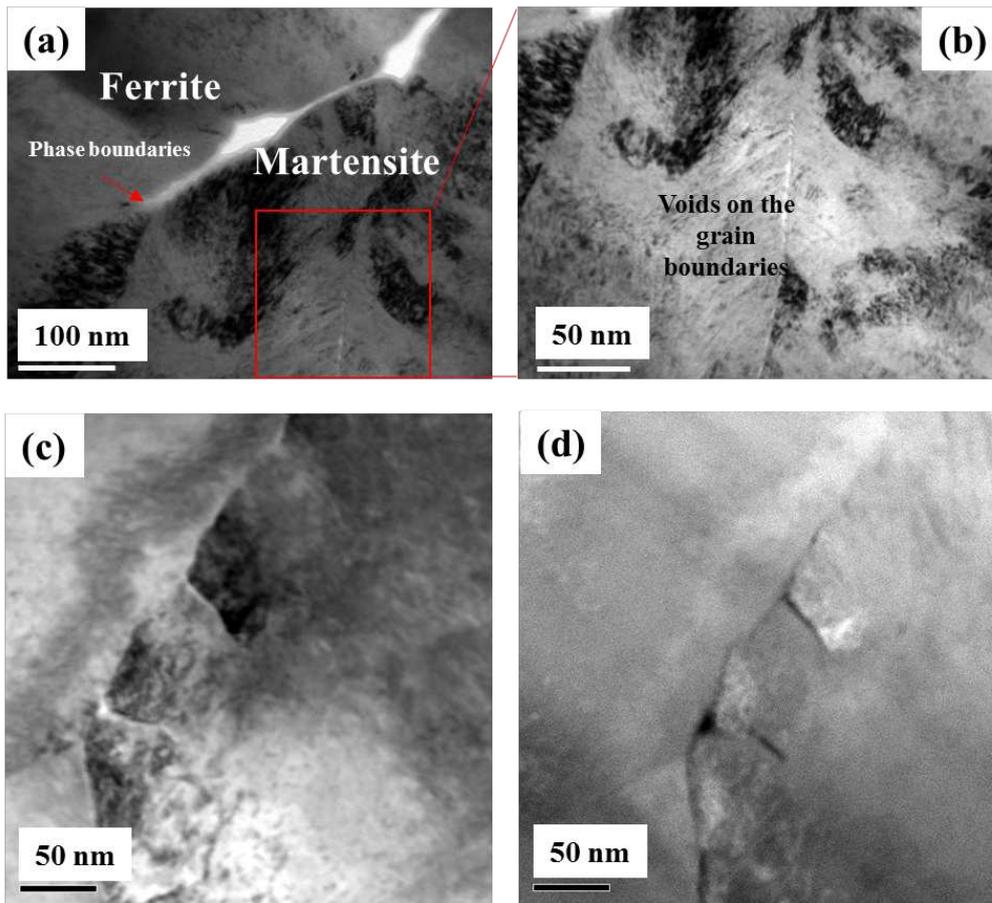
Fig. 17. Micrographs of voids in the V-Mo steel after hydrogen charging from FIB lift out TEM samples from the tensile fracture surfaces in regions where martensite was present showing: (a) voiding along a ferrite/martensite phase boundaries; (b) TEM bright field image of voiding along a martensite lath boundary shown in (a); (c) and (d) STEM bright and dark field images from a ferrite triple junction showing extensive voiding.
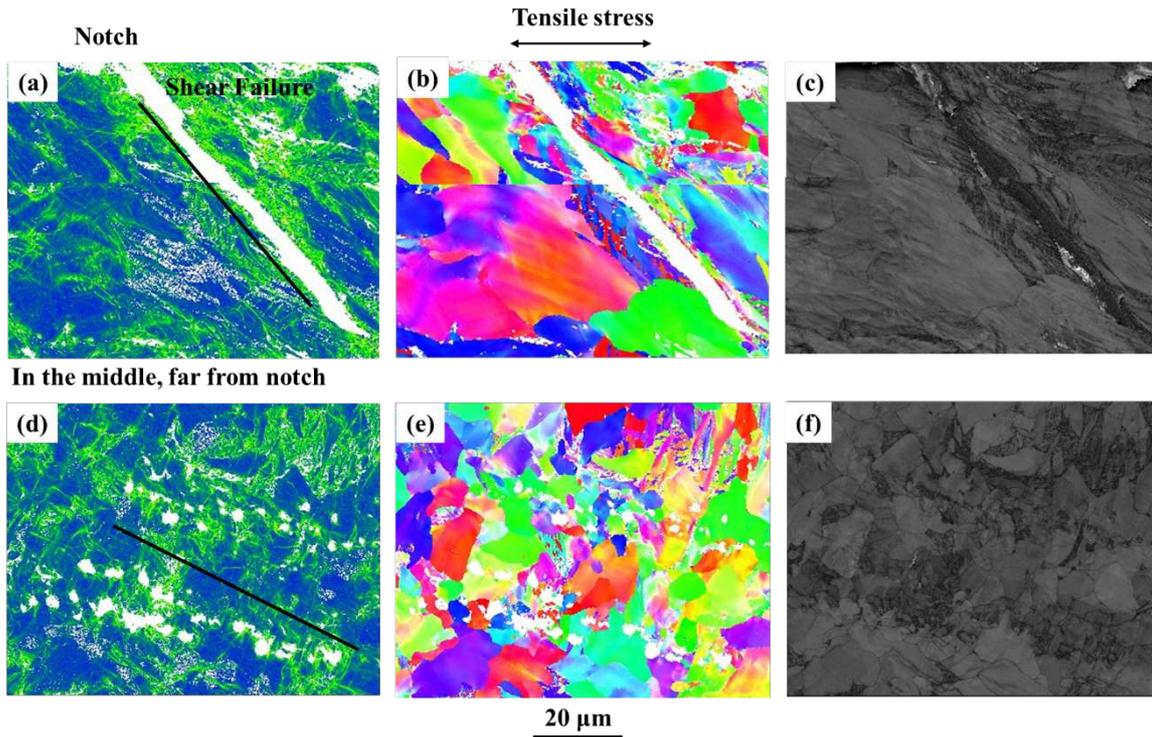
Fig. 18. EBSD map from uncharged V-Mo steel: (a-c) taken from the notched area (a) KAM map; (b) IPF map and (c) BC map; and (d-f) taken far from the notched area (d) KAM map; (e) IPF map and (f) BC map.
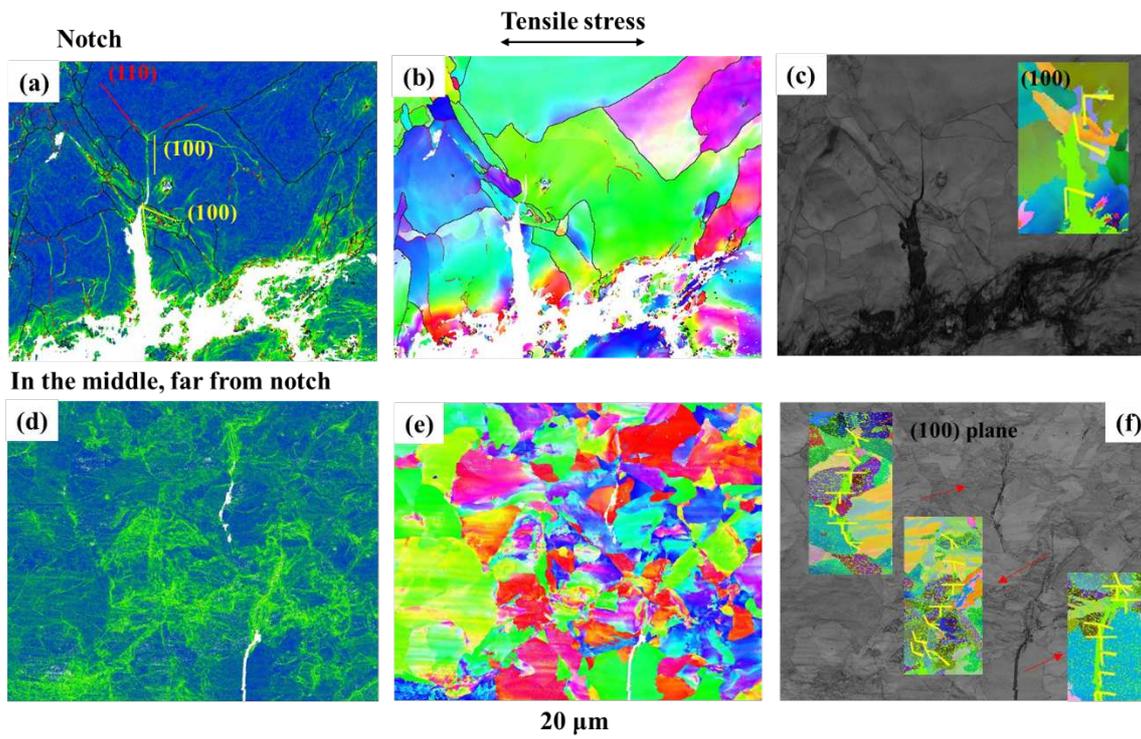

Fig. 19. EBSD map showing that the crack growth through in the ferrite grains along the (100) plane in the charged Ti-Mo steel: (a-c) taken from the notched area, (a) KAM map; (b) IPF map; (c) BC map; (d-f) showing secondary cracking away from the notch with traces of (100) marked on (d) KAM map; (e) IPF map; (f) BC map.
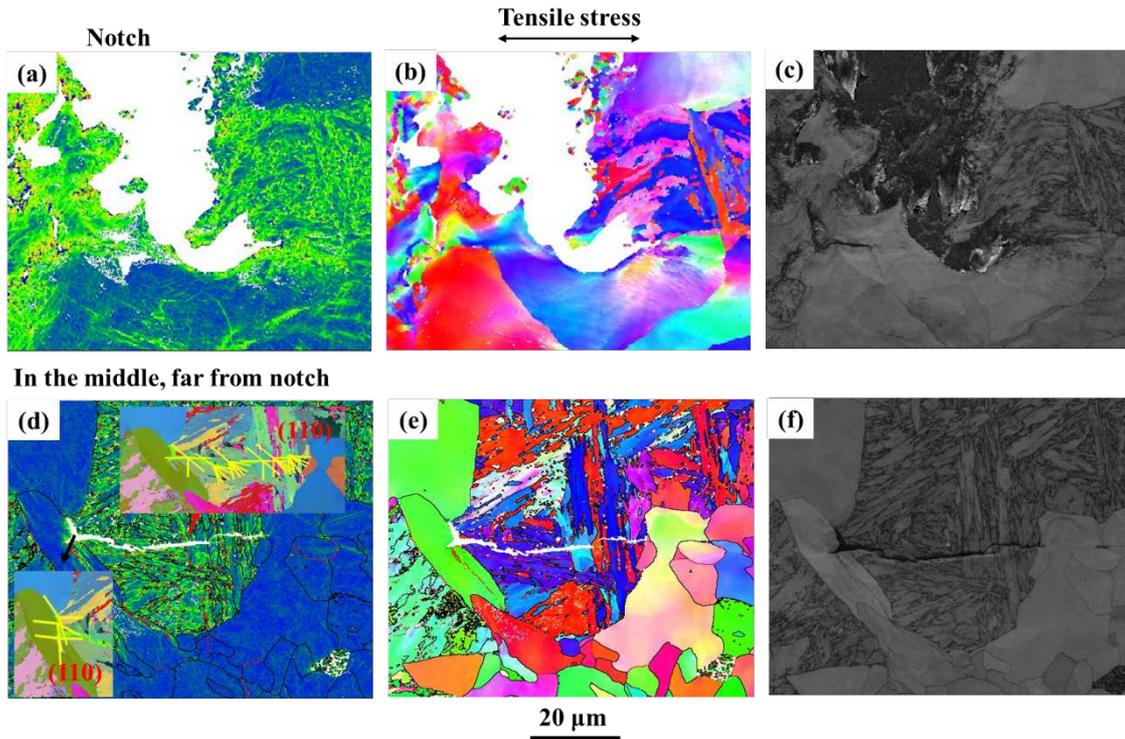
Fig. 20. EBSD maps of the charged V-Mo steel, showing that the crack growth along the ferrite/martensite boundary: (a-c) taken from the notched area, (a) KAM map showing the root of the notch, with the main crack propagating parallel to the tensile axis, into a martensite island; (b) IPF map; (c) BC map; (d-f) showing secondary cracking away from the notch propagating vertical to the tensile axis with traces of (110) marked on, (d) KAM map, (e) IPF map, (f) BC map.